Monthly Notices of the ROYAL ASTRONOMICAL SOCIETY

MNRAS **529,** 4914–4928 (2024) https://doi.org/10.1093/mnras/stae850
Advance Access publication 2024 March 26

Origin of the correlation between stellar kinematics and globular cluster system richness in ultradiffuse galaxies

Joel Pfeffer [1,2]★ Steven R. Janssens [1,2] Maria Luisa Buzzo [1,2] Jonah S. Gannon [1,2] Nate Bastian,[3,4] Kenji Bekki,[5] Jean P. Brodie,[1,2,6] Warrick J. Couch,[1] Robert A. Crain [7] Duncan A. Forbes,[1,2] J. M. Diederik Kruijssen [8,9] and Aaron J. Romanowsky [10,11]

[1]*Centre for Astrophysics & Supercomputing, Swinburne University, Hawthorn, VIC 3122, Australia*
[2]*ARC Centre of Excellence for All Sky Astrophysics in 3 Dimensions (ASTRO 3D), Canberra, ACT 2611, Australia*
[3]*Donostia International Physics Center (DIPC), Paseo Manuel de Lardizabal, 4, E-20018 Donostia-San Sebastián, Guipuzkoa, Spain*
[4]*IKERBASQUE, Basque Foundation for Science, E-48013 Bilbao, Spain*
[5]*International Centre for Radio Astronomy Research, University of Western Australia, 35 Stirling Highway, Crawley, WA 6009, Australia*
[6]*University of California Observatories, 1156 High Street, Santa Cruz, CA 95064, USA*
[7]*Astrophysics Research Institute, Liverpool John Moores University, 146 Brownlow Hill, Liverpool L3 5RF, UK*
[8]*Technical University of Munich, School of Engineering and Design, Department of Aerospace and Geodesy, Chair of Remote Sensing Technology, Arcisstr. 21, D-80333 Munich, Germany*
[9]*Cosmic Origins Of Life (COOL) Research DAO, coolresearch.io*
[10]*Department of Physics and Astronomy, San José State University, One Washington Square, San Jose, CA 95192, USA*
[11]*Department of Astronomy & Astrophysics, University of California Santa Cruz, 1156 High Street, Santa Cruz, CA 95064, USA*

Accepted 2024 March 21. Received 2024 March 1; in original form 2023 December 13

ABSTRACT

Observational surveys have found that the dynamical masses of ultradiffuse galaxies (UDGs) correlate with the richness of their globular cluster (GC) system. This could be explained if GC-rich galaxies formed in more massive dark matter haloes. We use simulations of galaxies and their GC systems from the E-MOSAICS project to test whether the simulations reproduce such a trend. We find that GC-rich simulated galaxies in galaxy groups have enclosed masses that are consistent with the dynamical masses of observed GC-rich UDGs. However, simulated GC-poor galaxies in galaxy groups have higher enclosed masses than those observed. We argue that GC-poor UDGs with low stellar velocity dispersions are discs observed nearly face on, such that their true mass is underestimated by observations. Using the simulations, we show that galactic star formation conditions resulting in dispersion-supported stellar systems also leads to efficient GC formation. Conversely, conditions leading to rotationally supported discs lead to inefficient GC formation. This result may explain why early-type galaxies typically have richer GC systems than late-type galaxies. This is also supported by comparisons of stellar axis ratios and GC-specific frequencies in observed dwarf galaxy samples, which show GC-rich systems are consistent with being spheroidal, while GC-poor systems are consistent with being discs. Therefore, particularly for GC-poor galaxies, rotation should be included in dynamical mass measurements from stellar dynamics.

Key words: methods: numerical – globular clusters: general – galaxies: evolution – galaxies: formation – galaxies: kinematics and dynamics.

1 INTRODUCTION

Although dwarf galaxies (stellar masses $M_* \lesssim 10^9\,\mathrm{M}_\odot$) only make up a small fraction of the present-day stellar mass density, they are the most numerous type of galactic system in the Universe (Li & White 2009). Their properties (e.g. being dark-matter-dominated systems) make them strong probes of both galaxy formation and cosmological models (see Sales, Wetzel & Fattahi 2022, for a recent review).

Recent years have seen considerable interest in a population of dwarf galaxies with large sizes ($R_{\rm eff} \gtrsim 1.5$ kpc) and low central surface brightness ($\mu_{\rm g,0} \gtrsim 24\,\mathrm{mag\,arcsec^{-2}}$), typically termed ultradiffuse galaxies (UDGs, van Dokkum et al. 2015a). Since their identification in the Coma cluster (van Dokkum et al. 2015a, b), UDGs have also been discovered in other clusters, galaxy groups and field environments (e.g. Martínez-Delgado et al. 2016; van der Burg, Muzzin & Hoekstra 2016; Janssens et al. 2017; Leisman et al. 2017; Román & Trujillo 2017; La Marca et al. 2022; Zaritsky et al. 2023). Their half-light radii are considerably larger than other early-type dwarf galaxies with similar stellar masses, which typically have sizes $R_{\rm eff} \lesssim 1$ kpc (e.g. Misgeld & Hilker 2011; McConnachie 2012), though some late-type galaxies of similar mass have comparable sizes, (Hunter & Elmegreen 2006; Baldry et al. 2012). Thus, the stellar dynamics of UDGs can probe dynamical masses to larger

★ E-mail: jpfeffer@swin.edu.au

physical radii compared to 'classical' early-type dwarf galaxies of similar stellar mass (approaching radii reached by H I discs), enabling stronger tests of the dark matter content of such gas-free galaxies.

Kinematic measurements, using both stellar and globular cluster (GC) system dynamics, have revealed a wide range in the dark matter mass content of UDGs, from dark matter-dominated systems (Beasley et al. 2016; van Dokkum et al. 2016; Toloba et al. 2018; Martín-Navarro et al. 2019; van Dokkum et al. 2019b; Gannon et al. 2020; Forbes et al. 2021; Gannon et al. 2021, 2022, 2023; Toloba et al. 2023) to dark matter-deficient systems (NGC1052-DF2 and NGC1052-DF4, van Dokkum et al. 2018a; Danieli et al. 2019; Emsellem et al. 2019; van Dokkum et al. 2019a; Müller et al. 2020; Shen, van Dokkum & Danieli 2023). Similarly, for field UDGs with H I discs, measurements of their rotation curves yield estimates from them residing in normal dwarf galaxy-mass haloes (halo virial masses $M_{200} \approx 10^{10.5}$-$10^{11}$ $M_{\odot}$, Leisman et al. 2017; Shi et al. 2021) to being baryon-dominated systems (Mancera Piña et al. 2019; Kong et al. 2022; Mancera Piña et al. 2022), with the largest source of uncertainty being the inclination of the systems. In edge-on systems, where the inclination correction is minimal, the H I velocity widths are consistent with the galaxies residing in typical dwarf galaxy–mass haloes (He et al. 2019, see Section 3.2).

Related to their dynamical mass measurements is whether individual UDGs of similar stellar mass obey the scaling between dark matter halo mass and total GC mass or number (Blakeslee, Tonry & Metzger 1997; Blakeslee 1999; Spitler & Forbes 2009; Harris, Harris & Alessi 2013; Harris, Blakeslee & Harris 2017; Burkert & Forbes 2020). UDGs have been found to host a wide range of GC numbers, including some with significantly more GCs than normal dwarf galaxies of similar luminosity (e.g. Beasley & Trujillo 2016; van Dokkum et al. 2017; Amorisco et al. 2018; Lim et al. 2018; Forbes et al. 2020; Lim et al. 2020; Danieli et al. 2022). Such rich GC systems might indicate the galaxies formed in 'overmassive' dark matter haloes (Beasley et al. 2016; Toloba et al. 2023; Forbes & Gannon 2024), or, equivalently, formed less stellar mass than expected for their halo mass (often referred to as the 'failed galaxy' scenario, e.g. van Dokkum et al. 2015a; Forbes et al. 2020). Generally, reconciling dynamical mass measurements with the GC number-halo mass relation requires such galaxies to reside in cored dark matter haloes (Gannon et al. 2022, 2023). The formation of dark matter cores due to outflows driven by stellar feedback (e.g. Navarro, Eke & Frenk 1996a; Read & Gilmore 2005; Governato et al. 2010; Macciò et al. 2012; Pontzen & Governato 2012) may also be a process that results in the formation of UDGs (e.g. Di Cintio et al. 2017; Chan et al. 2018; Carleton et al. 2019; Martin et al. 2019; Trujillo-Gomez et al. 2021; Trujillo-Gomez, Kruijssen & Reina-Campos 2022).

Recently, Gannon et al. (2022) found that UDGs in the Perseus cluster with few GCs have lower stellar velocity dispersions (lower dynamical masses) than those with rich GC systems. This would be expected if they follow the N_{GC}–M_{200} relation, and would imply haloes that have efficiently formed stars (i.e. low M_{200} for a fixed M_*) have either less efficiently formed GCs, or preferentially disrupted them. Alternatively, the radial profile of haloes could differ between GC-rich and GC-poor galaxies (e.g. if GC-rich galaxies are formed in high-concentration haloes, Trujillo-Gomez et al. 2022). There are also outliers such as NGC1052-DF2 and NGC1052-DF4, which have low dynamical masses but high GC luminosity fractions (van Dokkum et al. 2018b, 2019a). Such dark matter-deficient galaxies could perhaps form due to tidal stripping of their dark matter haloes by nearby massive galaxies (Safarzadeh & Scannapieco 2017; Ogiya 2018; Jing et al. 2019; Doppel et al. 2021; Jackson et al. 2021; Macciò et al. 2021; Moreno et al. 2022; Ogiya, van den Bosch & Burkert 2022), but may require alternative formation scenarios (e.g. tidal dwarf galaxies, Bournaud et al. 2007; Lelli et al. 2015; Román et al. 2021; Poulain et al. 2022; dwarf galaxy collisions, Silk 2019; Shin et al. 2020; Lee, Shin & Kim 2021; van Dokkum et al. 2022; expansion due to GC feedback, Trujillo-Gomez et al. 2022). Explanations of dynamical differences between GC-rich and GC-poor galaxies must therefore also take into account the environment in which the galaxies reside, given GC-rich UDGs are often found in galaxy clusters, while isolated field UDGs have very few GCs (Jones et al. 2023).

In this work, we use simulations of galaxies from the E-MOSAICS project (MOdelling Star cluster population Assembly In Cosmological Simulations within EAGLE, Pfeffer et al. 2018; Kruijssen et al. 2019a) to explore alternative explanations for the relationship between inferred dynamical mass and GC numbers. First, we consider whether differing formation histories of galaxies also result in differing dynamical masses. Cluster galaxies may have truncated formation histories due to early infall times and subsequent quenching. Therefore, the mass profiles of their dark matter haloes may be more related to those at higher redshifts, which have lower concentrations but are more compact due to their smaller virial radii (e.g. Bullock et al. 2001). If GC richness correlates with infall redshift (e.g. Mistani et al. 2016; Carleton et al. 2021), then a correlation between GC richness and dynamical mass may be expected. Any of these scenarios may be affected by the tidal stripping of dark matter haloes within group/cluster environments, thus this effect must also be taken into account.

We also consider whether the dynamics of GC-rich and GC-poor galaxies are systematically different, leading to differing inferred dynamical masses. We suggest that differing formation histories of galaxies may lead to a correlation between GC richness and the amount of dispersion support in the host galaxy. Galaxies with low-velocity dispersions (typically GC-poor galaxies) could be oblate discs observed at low inclinations, such that mainly the vertical motions in the disc contribute to the stellar velocity dispersions, while GC-rich galaxies are largely dispersion supported.

This paper is ordered as follows. In Section 2, we briefly describe the E-MOSAICS simulations and galaxy selection. Section 3 presents the main results of this work on correlations between GC system richness and galaxy enclosed masses/kinematics. Section 4 discusses comparisons of the results of this work with observed galaxies and implications for the formation of UDGs. Finally, the key results of this work are summarized in Section 5.

2 METHODS

In this section, we briefly describe the galaxy and GC formation simulation used in this work (Section 2.1), selection of galaxies and GCs from the simulation (Section 2.2) and spurious numerical effects that impact analysis of the simulation (Section 2.3).

2.1 E-MOSAICS simulation

The E-MOSAICS project (Pfeffer et al. 2018; Kruijssen et al. 2019a) is a suite of cosmological hydrodynamical simulations, based on the EAGLE (Evolution and Assembly of GaLaxies and their Environments) galaxy formation model (Crain et al. 2015; Schaye et al. 2015), which incorporates subgrid models for the formation and evolution of stellar clusters (MOSAICS, Kruijssen et al. 2011; Pfeffer et al. 2018). Here, we only briefly describe the EAGLE and

E-MOSAICS models, and refer interested readers to the above works for full details.

EAGLE is a suite of cosmological hydrodynamical simulations of galaxy formation and evolution with a Lambda cold dark matter cosmogony (Crain et al. 2015; Schaye et al. 2015) whose data have been released to the community (McAlpine et al. 2016). The simulations adopt cosmological parameters that are consistent with those inferred by the Planck Collaboration XVI (2014), namely $\Omega_\mathrm{m} = 0.307$, $\Omega_\Lambda = 0.693$, $\Omega_\mathrm{b} = 0.04825$, $h = 0.6777$, and $\sigma_8 = 0.8288$. The simulations are performed with a highly modified version of the *N*-body Tree-PM smoothed particle hydrodynamics code GADGET3 (last described by Springel 2005). The EAGLE model includes subgrid routines describing element-by-element radiative cooling (Wiersma, Schaye & Smith 2009a), pressure-dependent star formation that reproduces the observed Kennicutt (1998) star formation law (Schaye & Dalla Vecchia 2008), stellar evolution and stellar mass-loss (Wiersma et al. 2009b), the growth of supermassive black holes through gas accretion and mergers (Rosas-Guevara et al. 2015) and feedback associated with both star formation and black hole growth (Booth & Schaye 2009). The simulations lack the resolution and physics to model the cold, dense phase of the interstellar medium. Therefore, to prevent artificial fragmentation, cold and dense gas is not allowed to cool below temperatures corresponding to an equation of state $P_\mathrm{eos} \propto \rho^{4/3}$, normalized to $T_\mathrm{eos} = 8000\,\mathrm{K}$ at $n_\mathrm{H} = 10^{-1}\,\mathrm{cm}^{-3}$. To ensure the emergence of a realistic galaxy population, the parameters governing star formation and black hole feedback were calibrated to reproduce the present-day galaxy stellar mass function, the sizes of disc galaxies and black hole-stellar mass relation (Crain et al. 2015). The EAGLE simulations have been shown to broadly reproduce a wide variety of observables, including the Tully–Fisher relation and passive galaxy fractions (Schaye et al. 2015), the evolution of the galaxy stellar mass function (Furlong et al. 2015) and galaxy sizes (for normal galaxies with $M_* \gtrsim 10^{9.5}\,\mathrm{M}_\odot$, Furlong et al. 2017), cold gas properties (Lagos et al. 2015; Crain et al. 2017), galaxy star formation rates and colours (Furlong et al. 2015; Trayford et al. 2017) and galaxy morphologies (Bignone et al. 2020; Pfeffer et al. 2023a).

Galaxies (subhaloes) are identified in the simulation using the two-part method described by Schaye et al. (2015). First, dark matter structures are identified using the friends-of-friends (FOF) algorithm (Davis et al. 1985). Next, bound substructures (subhaloes/galaxies) are then identified using the SUBFIND algorithm (Springel et al. 2001; Dolag et al. 2009). The galaxy in each FOF group containing the particle with the lowest gravitational potential is considered to be the *central* galaxy, while all others are considered to be *satellite* galaxies. Galaxy merger trees were constructed from the subhalo catalogues using the D-TREES algorithm (Jiang et al. 2014; Qu et al. 2017). We use the merger trees to determine the infall redshift for each satellite galaxy. We define infall redshift as the first snapshot redshift, after reaching peak subhalo mass as a central, at which a galaxy becomes a satellite. The requirement for reaching peak mass excludes cases where a galaxy may only briefly be considered a satellite during early major mergers.

The MOSAICS star cluster model (Kruijssen et al. 2011; Pfeffer et al. 2018) is coupled to the EAGLE model by treating star clusters as subgrid components of baryonic particles. Each star particle may host its own subgrid population of star clusters, which is created at the time of star formation (i.e. when a gas particle is converted into a star particle). The star clusters then form and evolve according to local properties within the simulation (i.e. local gas and dynamical properties) and adopt the properties of the host particle (i.e. positions, velocities, ages, and abundances). Star cluster formation is determined by two properties: the cluster formation efficiency (CFE, i.e. the fraction of stars formed in bound clusters, Bastian 2008) and the shape of the initial cluster mass function (a power law or a Schechter 1976 function with a high-mass exponential truncation, $M_{\mathrm{c},*}$). In the fiducial E-MOSAICS model, the CFE is determined by the Kruijssen (2012) model (where CFE scales with local gas pressure), while $M_{\mathrm{c},*}$ is determined by the Reina-Campos & Kruijssen (2017) model (where $M_{\mathrm{c},*}$ increases with local gas pressure, except in regions limited by high Coriolis or centrifugal forces). Star cluster formation within each particle is treated stochastically, such that the subgrid clusters may be more massive than the host particle and the mass is conserved only for an ensemble of star particles (for details, see Pfeffer et al. 2018). After formation, star clusters lose mass by stellar evolution (following the EAGLE model), two-body relaxation that depends on the local tidal field strength (Lamers et al. 2005; Kruijssen et al. 2011) and tidal shocks from rapidly changing tidal fields (Gnedin, Hernquist & Ostriker 1999; Prieto & Gnedin 2008; Kruijssen et al. 2011). The complete disruption of clusters by dynamical friction (i.e. assuming they merge to the centre of their host galaxy) is treated in post-processing at every snapshot (Pfeffer et al. 2018).

This work discusses galaxies from the E-MOSAICS simulation of a periodic cube with side-length $L = 34.4$ comoving Mpc (Bastian et al. 2020). The simulation initially has 2×1034^3 particles, using an equal number of baryonic and dark matter particles, with dark matter particle masses of $1.21 \times 10^6\,\mathrm{M}_\odot$ and initial gas particle masses of $2.26 \times 10^5\,\mathrm{M}_\odot$. The simulation uses a gravitational softening length fixed in comoving units (1.33 comoving kpc) until $z = 2.8$, and in proper units (0.35 kpc) thereafter. The simulation was performed using the 'recalibrated' EAGLE model (see Schaye et al. 2015). Though four-star cluster formation models are simulated in parallel (setting both the CFE and $M_{\mathrm{c},*}$ to be constant or environmentally varying, see Bastian et al. 2020), this work focuses on the fiducial E-MOSAICS model (with environmentally varying star cluster formation). The fiducial E-MOSAICS model produces star cluster populations which are broadly consistent with many observed relations, including the 'blue tilt' of GC colour distributions (Usher et al. 2018), the age–metallicity relations of GC systems (Kruijssen et al. 2019b, 2020; Horta et al. 2021), the radial distributions of GC systems (Kruijssen et al. 2019a; Reina-Campos et al. 2022), the scaling relations of young star clusters (Pfeffer et al. 2019b), the fraction of stars contained in GCs (Bastian et al. 2020), the UV luminosity function of high-redshift proto-GCs (Pfeffer et al. 2019a; Bouwens et al. 2021), the high-mass truncation of GC mass functions (Hughes et al. 2022) and the metallicity distributions of GC systems (Pfeffer et al. 2023b). However, as discussed in detail by Pfeffer et al. (2018) and Kruijssen et al. (2019a), the simulations overpredict the number of low-mass and high-metallicity GCs, which is likely a consequence of insufficient disruption of GCs by tidal shocks due to an overly smooth interstellar medium in the simulations (EAGLE does not model the cold, dense interstellar medium phase, see Schaye et al. 2015).

2.2 Galaxy and GC selection

We select dwarf galaxies with stellar masses in the range $2 \times 10^8 < M_*/\mathrm{M}_\odot < 6 \times 10^8$, giving 501 galaxies at $z = 0$ (188 are satellites galaxies, 73 are satellite galaxies in haloes with $M_{200} > 10^{13}\,\mathrm{M}_\odot$). The mass range is chosen to be similar to the stellar masses of galaxies in Gannon et al. (2022). At the resolution of the simulation (and factoring in stellar-evolutionary mass-loss for the particles), the mass limits select galaxies with ≈1500–5000 stellar particles. Such

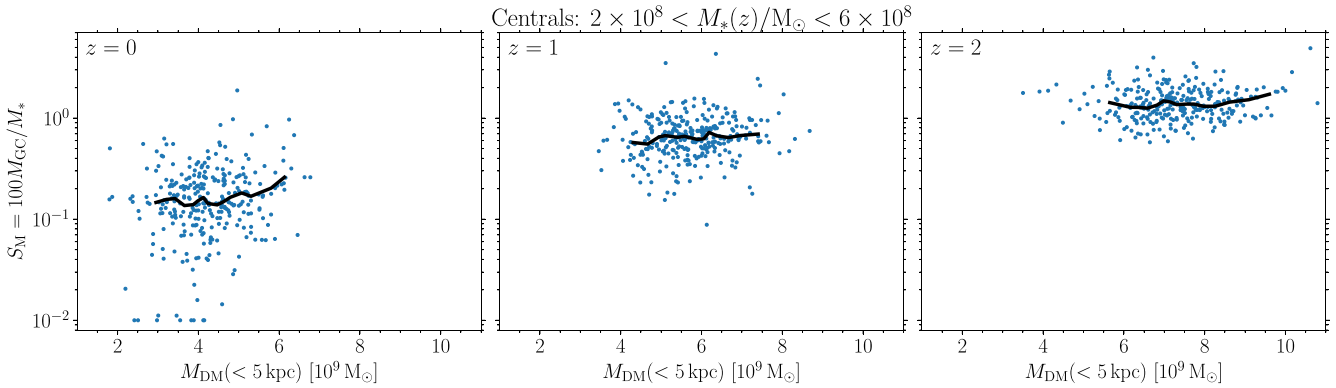

Figure 1. GC-specific masses (S_M) compared with enclosed dark matter mass within 5 kpc for central dwarf galaxies in the E-MOSAICS simulation. The panels show galaxies with stellar masses $2 \times 10^8 < M_*(z)/\,\mathrm{M}_\odot < 6 \times 10^8$ at different redshifts ($z = 0$, 1, 2 in the left, middle, and right panels, respectively). Galaxies with specific masses below the plotted range are shown at $S_\mathrm{M} = 1 \times 10^{-2}$ (all of these galaxies have $S_\mathrm{M} = 0$). Note that the axis limits are identical in each panel so they may be directly compared. Only weak correlations are found between S_M and $M_\mathrm{DM}(< 5\,\mathrm{kpc})$ at all redshifts (Spearman correlation coefficients $\approx$0.1, with p-values $\approx$0.1), indicating that correlations between enclosed mass within 5 kpc and GC richness are not expected in the E-MOSAICS model.

galaxies are typically formed in dark matter haloes with masses $\approx 10^{10.7}\,\mathrm{M}_\odot$ in the simulation. We do not select galaxies by size or surface brightness, given that dwarf galaxies in EAGLE simulations are already generally too large and have typical sizes comparable with UDGs (projected half-mass radii $R_{50} \approx 2$ kpc, Schaye et al. 2015). This is a result of numerical limitations in the simulations, i.e. the temperature floor for dense gas, which artificially thickens discs (Benítez-Llambay et al. 2018), and spurious heating from interactions of stellar and dark matter particles (Ludlow et al. 2019, see also following section).

E-MOSAICS models GC formation assuming both young and old star clusters form via a common mechanism. Therefore, to compare populations of GCs, we select star clusters with masses $> 10^{4.5}\,\mathrm{M}_\odot$ and ages > 2 Gyr at $z = 0$ (i.e. clusters that have already undergone significant mass-loss through stellar evolution). All such star clusters that are bound to a galaxy (subhalo) according to SUBFIND are taken to be part of the galaxy's GC population.

2.3 Galaxy dynamics and spurious heating

We elect not to directly investigate the stellar kinematics of dwarf galaxies in the simulation, as they are affected by the spurious heating of stellar orbits by interactions with dark matter particles. This process will occur in any simulation when dark matter particles are significantly more massive than baryonic particles (Ludlow et al. 2019, 2021, 2023; Wilkinson et al. 2023). Galaxies affected by spurious heating become larger and rounder, and the stellar dynamics becomes more dispersion supported. By contrast, the effect on the dark matter profiles is significantly smaller, with a slight increase in halo concentration within the stellar half-mass radius due to the mass segregation of the more massive dark matter particles (Ludlow et al. 2019). Older galaxies will be more affected by spurious heating than younger galaxies, given the longer time-scale for heating to occur. For the particle masses of the EAGLE high-resolution model, this particularly affects galaxies in haloes with masses $M_{200} \lesssim 10^{12}\,\mathrm{M}_\odot$ (Ludlow et al. 2021).

Therefore, we instead investigate the dynamics of 'star-forming' gas in the simulation, for which the limiting factor is the radiative cooling model. EAGLE does not model the cold gas phase, and instead has a polytropic equation of state $P_\mathrm{eos} \propto \rho^{4/3}$ with a temperature floor at 8×10^3 K (Schaye et al. 2015). The cooling floor implies a velocity dispersion floor that increases weakly with density/pressure ($\sigma \approx [13, 17, 23]\,\mathrm{km\,s^{-1}}$ at $P/k = [10^3, 10^4, 10^5]\,\mathrm{K\,cm^{-3}}$). This is slightly higher than the stellar velocity dispersion found for NGC1052-DF2 and DF4 (Danieli et al. 2019; Emsellem et al. 2019; Shen et al. 2023), but is generally smaller than the velocity dispersions of normal dwarf galaxies with stellar masses between 10^8 and $10^9\,\mathrm{M}_\odot$, which have stellar velocity dispersions in the range 20–100 $\mathrm{km\,s^{-1}}$ (e.g. Norris et al. 2014).

3 RESULTS

3.1 Enclosed dark matter masses and GC system richness

In Fig. 1, we first compare the relationship between GC-specific mass (the ratio of total GC mass and galaxy stellar mass, $S_\mathrm{M} = 100 M_\mathrm{GC}/M_*$) and dark matter mass ($M_\mathrm{DM}$) within 5 kpc for central dwarf galaxies (i.e. excluding satellites of larger haloes) at different redshifts. Such a correlation might be expected if S_M depends on the halo concentration.[1] or M_*/M_{200}. The radius limit of 5 kpc was chosen to be similar to the dynamical mass measurements of UDGs (e.g. Gannon et al. 2022), however, the correlations for 3 and 10 kpc radii are nearly identical to the 5 kpc limit. The comparison is limited to only central galaxies so that effects from the tidal stripping of dark matter haloes are excluded. Galaxies are selected within the same stellar mass range ($2 \times 10^8 < M_*(z)/\,\mathrm{M}_\odot < 6 \times 10^8$) at each redshift (i.e. the figure does not show an evolutionary sequence). At all redshifts ($z = 0$, 1, and 2), there are only weak correlations between S_M and $M_\mathrm{DM}(< 5\,\mathrm{kpc})$, having Spearman correlation coefficients $\approx$0.1 (with p-values $\approx$0.1). Therefore, for dwarf galaxies in the E-MOSAICS simulations, differences in S_M at fixed M_* are not driven by differences in dark matter halo mass.

However, the typical values for both S_M and $M_\mathrm{DM}(< 5\,\mathrm{kpc})$ increase with redshift, with S_M increasing by a factor of $\sim$10 from $z = 0$ to 2, and $M_\mathrm{DM}(< 5\,\mathrm{kpc})$ increasing by a factor of $\sim$2. For the enclosed dark matter mass, this difference is because, at fixed halo mass, halo virial radii are smaller at earlier times, even though haloes

[1]For example, relative to a typical NFW halo concentration for our galaxies of $c_\mathrm{NFW} = 10$ and assuming fixed M_{200} and r_{200}, the enclosed dark matter mass within 5 kpc would decrease (increase) by a factor of 2 for $c_\mathrm{NFW} = 5$ ($c_\mathrm{NFW} = 20$). For an NFW halo, this relative difference becomes larger at smaller radii.

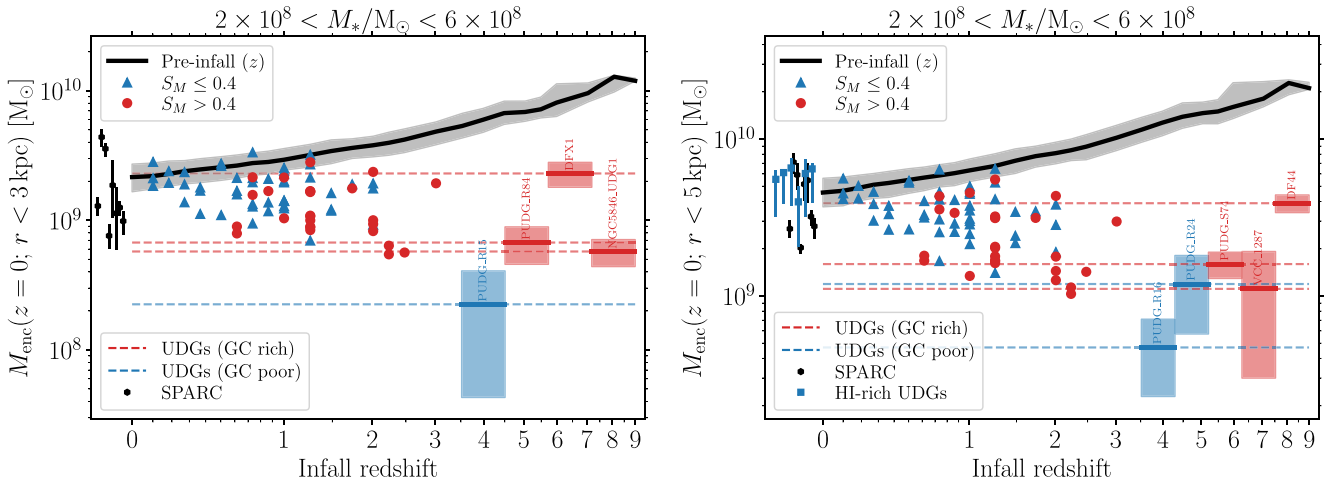

Figure 2. Enclosed masses within 3 kpc (left panel) and 5 kpc (right panel) at $z = 0$ as a function of infall redshift for E-MOSAICS dwarf galaxies in galaxy groups and clusters (FOF group mass $10^{13} < M_{200} \leq 10^{13.71}$ M$_\odot$). Red circles indicate GC-rich galaxies ($S_{\rm M} > 0.4$) while blue triangles show GC-poor galaxies ($S_{\rm M} < 0.4$). The median 'pre-infall' masses at each redshift (i.e. for central galaxies) are shown by the solid black line, with the grey-shaded region showing the 16$^{\rm th}$–84$^{\rm th}$ percentiles. Early infalling galaxies (which are typically GC rich) have lost more dark matter mass to tidal stripping than late infalling galaxies (which are typically GC poor). For comparison, the dashed lines (mean mass, shown the full redshift range to indicate unknown infall redshifts) and shaded regions (indicating 1σ uncertainties) show the dynamical masses from stellar velocity dispersions for GC-rich (red) and GC-poor (blue) UDGs from Gannon et al. (2022). The dynamical masses of GC-rich UDGs agree well with the masses of simulated GC-rich galaxies. The dynamical masses of GC-poor UDGs are generally significantly lower than those of simulated GC-poor galaxies. The blue squares (given H I-rich UDGs are GC poor, Jones et al. 2023) show the dynamical masses of edge-on H I-rich field UDGs (He et al. 2019). Black hexagons show the dynamical masses of normal H I-rich, high inclination ($i > 60°$) dwarf galaxies from SPARC (Lelli, McGaugh & Schombert 2016). Both samples of H I rich galaxies (the edge-on field UDGs and SPARC dwarfs) reasonably agree with the masses of $z \approx 0$ simulated galaxies, though with larger scatter in the observed samples.

are less concentrated (r_{200} decreases from ≈85 to 40 kpc from $z = 0$ to 2, while $c_{\rm NFW}$ decreases from ≈10 to 6). For the stellar mass range considered here, the total halo mass for galaxies at different redshifts is roughly constant ($M_{200} \approx 7 \times 10^{10}$ M$_\odot$) over the entire redshift range. The high $S_{\rm M}$ at earlier times is driven by the higher CFE due to higher natal gas pressure in the E-MOSAICS model (Pfeffer et al. 2018), as well as the young ages of clusters at high redshift which are yet to undergo significant mass-loss. In this stellar mass range, we expect at least a 0.5 dex decrease in $S_{\rm M}$ from initial to $z = 0$ values (Bastian et al. 2020). Thus, if the formation of a galaxy/halo was truncated at early times (e.g. via infall into a protocluster), the galaxy might plausibly have both elevated $S_{\rm M}$ and enclosed dark matter mass. In such a case, the galaxy would appear to reside in an 'overmassive' halo based on its enclosed mass, despite forming in a dwarf galaxy-mass halo ($M_{200} \approx 7 \times 10^{10}$ M$_\odot$). However, as we discuss in the next section, tidal stripping of dark matter haloes once they become satellites needs to be taken into account.

3.2 Enclosed masses and cluster infall times

The sample of UDGs with dynamical masses in Gannon et al. (2022) are from galaxy groups and clusters. Therefore, for comparison, we select E-MOSAICS dwarf galaxies which are satellites at $z = 0$ in the seven most massive FOF groups with $10^{13} < M_{200} \leq 10^{13.71}$ M$_\odot$. The most massive FOF group is limited by the simulation volume (34.4^3 Mpc^3), and therefore the simulation does not contain galaxy clusters as massive as the Perseus cluster ($M_{200} \approx 10^{15}$ M$_\odot$, Aguerri et al. 2020). The main impact is the volume is missing dwarf galaxies with infall redshifts >3, as higher mass haloes may have earlier infalling satellite galaxies (e.g. $z_{\rm infall} \lesssim 2$ for $M_{200} \lesssim 10^{12}$ M$_\odot$ and $z_{\rm infall} \lesssim 3$ for $M_{200} \lesssim 10^{13.7}$ M$_\odot$ for the dwarf galaxy mass range we consider, which would imply a maximum $z_{\rm infall} \approx 4$ for $M_{200} = 10^{15}$ M$_\odot$ if the scaling continues to higher masses).

In Fig. 2, we compare the total enclosed masses (i.e. sum of the masses of all gas, dark matter, stellar, and black hole particles) within 3 and 5 kpc at $z = 0$ for the E-MOSAICS dwarf galaxies as a function of the infall redshift (the redshift at which the galaxies become satellites in a larger halo). The radius limits are chosen to be similar to the effective radii range (2.7–5.2 kpc) for UDGs in the sample of Gannon et al. (2022). The galaxies are divided into 'GC-rich' (red circles) and 'GC-poor' (blue triangles) populations, with the division at a specific mass of $S_{\rm M} = 0.4$ (twice the typical value of $S_{\rm M}$ at $z = 0$, Fig. 1; which corresponds to the 20 GC limit used by Gannon et al. 2022 at $M_* = 5 \times 10^8$ M$_\odot$, assuming a typical GC mass of 10^5 M$_\odot$ for dwarf galaxies, Jordán et al. 2007). GC-rich galaxies typically have earlier infall redshifts ($z_{\rm infall} \gtrsim 1$) than GC-poor galaxies, as expected from the increase in $S_{\rm M}$ with redshift (Fig. 1; see also Mistani et al. 2016; Pfeffer et al. 2018; Carleton et al. 2021).

For comparison, the black line in Fig. 2 shows the pre-infall relation, i.e. the typical enclosed masses for central galaxies within the same stellar mass range at each snapshot. Although the enclosed masses for central galaxies increase with redshift (owing to more compact haloes, as discussed in Section 3.1), on average, the enclosed masses of satellite galaxies decrease with increasing infall redshift. This is due to tidal stripping of the dark matter haloes over time, which, interestingly, occurs at a faster rate than tidal stripping of the stellar component (e.g. for a galaxy which has lost half its stellar mass within 5 kpc, it will have lost ≈85 per cent of its dark matter mass within the same radius). The faster stripping of dark matter may be due to the radially biased orbits of dark matter haloes (e.g. Cole & Lacey 1996; Colín, Klypin & Kravtsov 2000). The impact of gas stripping on the enclosed masses is minor, as it typically only contributes ≈10 per cent of the pre-infall enclosed mass. This ratio is similar to that found for the SPARC galaxies (Lelli et al. 2016) shown in Fig. 2 (see below). Gas stripping is more important for

earlier infalling galaxies (approximately 40 per cent of the dwarf galaxies with $z_{\rm infall} \leq 1$ retain gas at $z = 0$, compared to ≈3 per cent with $z_{\rm infall} > 1$). In general, GC-rich simulated galaxies tend to have lower enclosed masses than GC-poor galaxies due to their earlier infall times (i.e. more time available for stripping of the dark matter haloes). Galaxies with infall redshifts $\lesssim 0.2$ have enclosed masses similar to central (isolated) galaxies at $z = 0$. Such late-infalling galaxies typically have group-/cluster-centric distances $\gtrsim R_{200}$.[2]

In Fig. 2, we also compare the inferred dynamical masses of UDGs from the sample compiled by Gannon et al. (2022). The sample is limited to galaxies with dynamical masses from stellar kinematics. For the UDG sample, the effective radii are in the range 2.7–5.2 kpc, and we assign the galaxies to the panel with the closest measurement radius (3 or 5 kpc). For observed galaxies the infall redshift is unknown, and thus the median measurement is indicated over the full redshift range. Overall, the enclosed masses from GC-rich simulated galaxies reasonably match the range from GC-rich UDGs. Thus, based on both their GC numbers and dynamical masses, GC-rich UDGs are consistent with being early-forming galaxies which have had much of their dark matter haloes stripped within the clusters. Most GC-rich UDGs in Gannon et al. (2022, NGC 5846 UDG1, PUDG R84, PUDG S74, and VCC 1287), as well as one GC-poor UDG (PUDG R24), have dynamical masses consistent with simulated galaxies with infall redshifts $z \approx$ 1–3. However, Gannon et al. (2022) noted that PUDG R24 has a disturbed morphology and is significantly bluer than other Perseus UDGs, which may indicate recent infall and quenching in the cluster. The GC-rich UDGs with the highest masses (DFX1 and DF44) have dynamical masses consistent with simulated galaxies over the full redshift range.

In contrast, the inferred masses of observed GC-poor UDGs are generally inconsistent with those of the GC-poor simulated galaxies, being a factor of 5–10 lower than expected from the simulations. Of the GC-poor UDGs, only PUDG R24 is consistent with the lowest enclosed masses found for simulated galaxies. Overall, the simulations predict the opposite trend to that found for observed UDGs, with GC-poor simulated galaxies typical having *higher* masses than GC-rich galaxies. For comparison with the $z \approx 0$ simulated galaxies, we include H I-rich dwarf galaxies ($2 \times 10^8 < M_*/{\rm M}_\odot < 6 \times 10^8$) with high inclinations ($i > 60$) from SPARC (*Spitzer* Photometry and Accurate Rotation Curves, Lelli et al. 2016), where dynamical masses were calculated from the H I rotation curves. The median dynamical masses from SPARC reasonably agree with the simulated galaxies, though with slightly larger scatter. In the right panel of Fig. 2, we also show dynamical masses for edge-on, H I-rich UDGs with $M_* > 10^8\,{\rm M}_\odot$ from He et al. (2019). Although other H I-rich UDGs also have measured H I rotational velocities, uncertainties in their inclination make their dynamical mass estimates highly uncertain (Karunakaran et al. 2020). We convert H I velocity widths to rotation velocities assuming that the galaxies are edge-on, then convert rotation velocities to dynamical masses assuming the peak rotation velocities are reached by 5 kpc.[3] In the uncertainties for the dynamical masses, we include an error on the inclination of 10° and a decrease in the velocity widths accounting for if the rotation velocity at 5 kpc is only 80 per cent of the peak velocity (e.g. as for AGC219533, Leisman et al. 2017). The GC-poor simulated galaxies with late infall times agree well with H I-rich field galaxies and UDGs, which host few GCs (Jones et al. 2023) and have dynamical masses expected for normal dwarf galaxies at $z = 0$.

As an alternative way to view the results in Fig. 2 (and a way to factor out the stellar mass differences between galaxies), in Fig. 3, we instead compare the enclosed stellar-to-enclosed mass ratios ($M_*/M_{\rm dyn}$) within 3 and 5 kpc as a function of group-/cluster-centric radius. Comparing stellar-to-enclosed mass ratios also helps to factor out differences in total mass as a function of stellar mass. For the observed galaxies, the enclosed stellar mass is taken to be half the total stellar mass, given the dynamical masses are estimated within the half-light radius (Gannon et al. 2022). The trends in Fig. 3 follow the trends in Fig. 2 for the simulated galaxies. Galaxies at smaller group-centric distances (earlier infall times) tend to be GC rich and have elevated $M_*/M_{\rm dyn}$ to central galaxies at $z = 0$. Galaxies at larger group-centric distances (later infall times) tend to be GC poor and have $M_*/M_{\rm dyn}$ that is similar to central galaxies at $z = 0$. For the galaxies with the highest stellar-to-enclosed mass ratios ($\gtrsim 0.2$), the mass ratios are not sensitive to the exact radius used, and the results are also similar for mass ratios within 10 kpc. The UDGs from Gannon et al. (2022) also generally follow the simulation trends, with those at the largest distances (DFX1 and DF44) having the lowest $M_*/M_{\rm dyn}$. Again, the GC-poor Perseus UDGs R15 and R16 are the largest outliers, having higher than expected $M_*/M_{\rm dyn}$ compared to the simulated GC-poor galaxies.

In the left panel of Fig. 3, we also show the dark matter-deficient UDGs NGC1052-DF2 (using the stellar velocity dispersions from both Danieli et al. 2019 and Emsellem et al. 2019) and NGC1052-DF4 (Shen et al. 2023). Dynamical masses were estimated using the same method as Gannon et al. (2022), i.e. using the mass estimator for dispersion-supported galaxies from Wolf et al. (2010). Given their projected distance to the elliptical galaxy NGC1052, we assume that both are members of the galaxy group, although note that tip of the red giant branch distance measurements may place one galaxy, or both, outside the group due to the relative distance of ≈ 2 Mpc between the UDGs (Shen et al. 2021). Both galaxies are taken to be GC rich given their high luminosity fraction in GCs (3-4 per cent, van Dokkum et al. 2018b, 2019a). The stellar-to-dynamical mass ratios for both NGC1052-DF2 and NGC1052-DF4 (≈0.6) are consistent with the highest mass ratios found in the simulations (≈0.4) within their uncertainties. In this case, the dark matter-deficient galaxies are consistent with tidal stripping of the dark matter halo (cf. Safarzadeh & Scannapieco 2017; Ogiya 2018; Jing et al. 2019; Doppel et al. 2021; Jackson et al. 2021; Macciò et al. 2021; Moreno et al. 2022; Ogiya et al. 2022). Both NGC1052-DF2 and NGC1052-DF4 have evidence of tidal distortions which would support such a scenario (Montes et al. 2020; Keim et al. 2022). If the UDGs reside outside the NGC1052 group (see Shen et al. 2021) then alternative formation scenarios are needed, such as galaxy collisions (Silk 2019; Shin et al. 2020; Lee et al. 2021; van Dokkum et al. 2022) or expansion through feedback from star cluster formation (Trujillo-Gomez et al. 2022).

Interestingly, the Perseus cluster GC-poor UDGs R15 and R16 have similar $M_*/M_{\rm dyn}$ to NGC1052-DF2 and NGC1052-DF4, as well as relatively small cluster-centric radii in projection ($r_{\rm clust}/R_{200} \approx 0.2$–0.3; which were selected to be matched in projected cluster-centric radii to other Perseus GC-rich UDGs, see Gannon et al. 2022). This could indicate both galaxies are also affected by significant tidal stripping of their dark matter haloes. However, the simulations show

[2]Though beyond the group 'virial radius' the galaxies at $r_{\rm group} > R_{200}$ are bound to the group. This simply indicates that a 1D radius may not describe well the triaxial shapes of massive haloes, such as recently merged groups or where the most bound/central galaxy is offset from the centre of mass.

[3]For dwarf galaxies in the SPARC sample with $10^8 < M_*/{\rm M}_\odot < 10^9$, around two-thirds of galaxies reach the flat part of the rotation curve by 5 kpc (Lelli et al. 2016).

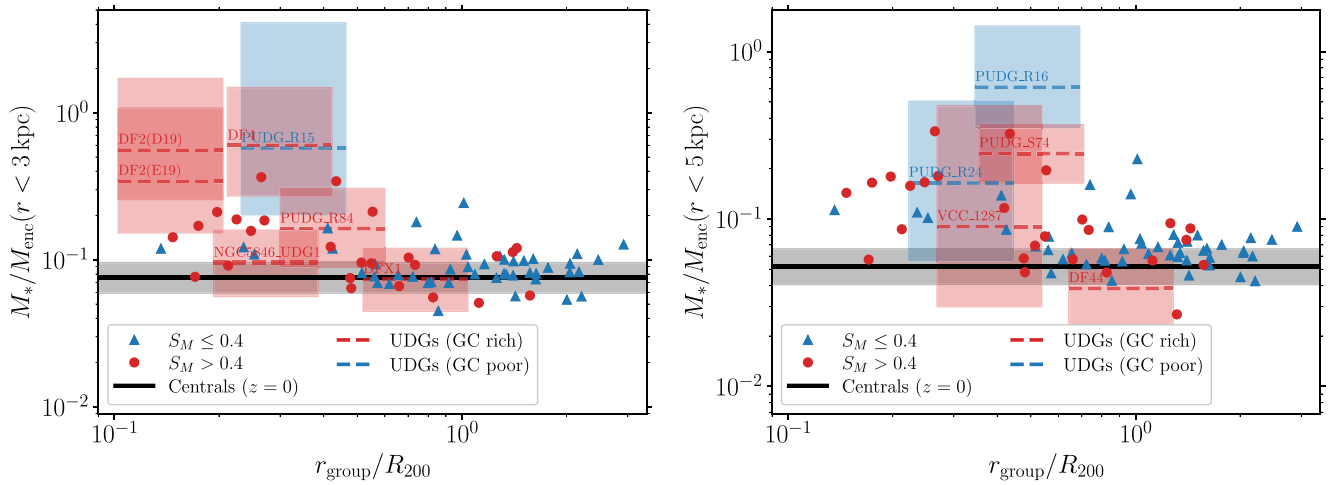

Figure 3. Stellar-to-enclosed mass ratios within 3 (left panel) and 5 kpc (right panel) as a function of group-/cluster-centric radius (distance to central galaxy of the FOF group, scaled by the group virial radius R_{200}) for the same galaxies in Fig. 2. Red circles indicate GC-rich galaxies ($S_{\rm M} > 0.4$) while blue triangles show GC-poor galaxies ($S_{\rm M} < 0.4$). For reference, the median mass ratios for central galaxies at $z = 0$ are shown by the solid black line, with the grey-shaded region showing the 16$^{\rm th}$–84$^{\rm th}$ percentiles, although we note that the mass ratio evolves with redshift (lower $M_*/M_{\rm dyn}$ at higher redshifts) as can be inferred from the higher pre-infall (central galaxy) dynamical masses in Fig. 2. The dashed lines (mean mass ratio) and shaded regions (indicating 1σ uncertainties) show the stellar-to-dynamical mass ratios for GC-rich (red) and GC-poor (blue) UDGs from Gannon et al. (2022), as well as NGC1052-DF2 (showing two mass estimates from velocity dispersion measurements from Danieli et al. 2019 and Emsellem et al. 2019) and NGC1052-DF4 (Shen et al. 2023). Group-/cluster-centric distances for observed galaxies are assumed to be uncertain by a factor of 2, with the minimum distance taken to be the projected distance from the central galaxy in the group/cluster (thus realistically, the distances for observed galaxies are only lower limits). The stellar mass-to-light ratios for observed galaxies are assumed to have an uncertainty of $\pm 0.5\,({\rm M/L})_\odot$.

this process is more likely to affect GC-rich galaxies, given their earlier infall times than GC-poor galaxies.

To summarize the results of this section, overall, the simulations agree well with the dynamical masses of both field galaxies and GC-rich group/cluster galaxies. In the latter case, this also suggests agreement in mass-loss from tidal stripping of galaxies and their dark matter haloes in groups/clusters. Therefore, disagreement in the enclosed and dynamical masses of GC-poor group/cluster galaxies between the simulations and observations likely have a different origin, which we explore in the following sections.

3.3 Dynamics of star-forming systems

Given that tidal stripping of dark matter haloes may not explain the dynamical masses of GC-poor UDGs in clusters, we now consider an alternative explanation: GC-poor dwarf galaxies are not dispersion-supported systems. In this case, the stellar velocity dispersions of observed GC-poor galaxies may underestimate the actual mass, depending on the inclination of the system. We suggest that galactic conditions leading to high-pressure star formation, and thus efficient GC formation, also lead to dispersion-supported stellar systems (spheroids). Conversely, conditions favouring low-pressure star formation (inefficient GC formation) instead lead to rotationally-supported discs. This may explain why early-type galaxies have richer GC systems than late-type galaxies (Georgiev et al. 2010).

In the E-MOSAICS model, the main difference between GC-rich and GC-poor dwarf galaxies is the natal gas pressures of star formation. We demonstrate this in Fig. 4, showing the relationship between $S_{\rm M}$ and median natal gas pressure in satellite dwarf galaxies. In the simulations, this relationship is due to the CFE scaling directly with the natal gas pressure (see Pfeffer et al. 2018). At low median pressures ($P/k \sim 10^{3.5}\,{\rm K\,cm^{-3}}$), there is significant scatter in $S_{\rm M}$ at a given median pressure due to factors such as temporal and

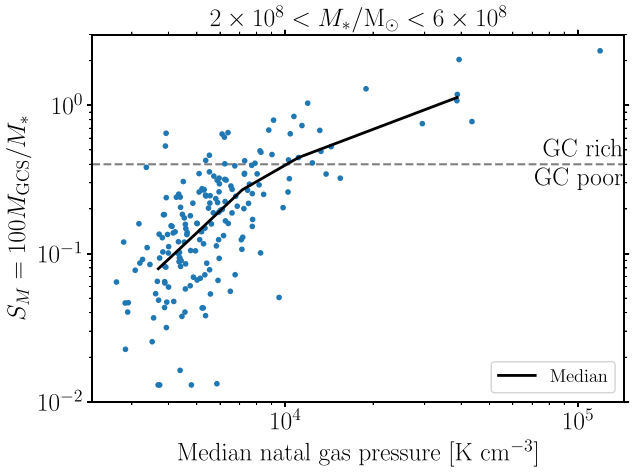

Figure 4. GC specific masses ($S_{\rm M}$) versus median natal gas pressure of stellar particles for E-MOSAICS satellite dwarf galaxies. The strong correlation between $S_{\rm M}$ and natal pressure is driven by the scaling of CFE with natal pressure in the E-MOSAICS model (Pfeffer et al. 2018). The transition from GC-poor ($S_{\rm M} < 0.4$) to GC-rich ($S_{\rm M} > 0.4$) galaxies occurs at $P/k \approx 10^4\,{\rm K\,cm^{-3}}$.

spatial variations in pressure and stochasticity in the GC formation model. Typically, galaxies become GC-rich ($S_{\rm M} > 0.4$) at a median $P/k \gtrsim 10^4\,{\rm K\,cm^{-3}}$.

Next, we turn to the connection between the gas pressure and dispersion-supported kinematics. To demonstrate this, in Fig. 5, we compare the dynamics of star-forming gas in the progenitors of galaxies with $2 \times 10^8 < M_*/\,{\rm M}_\odot < 6 \times 10^8$ at $z = 0$ (recalling that we compare gas kinematics, rather than stellar kinematics, due to the effect of spurious heating on stellar orbits, Section 2.3). Only central galaxies (at any redshift) are included to avoid effects such as tidal

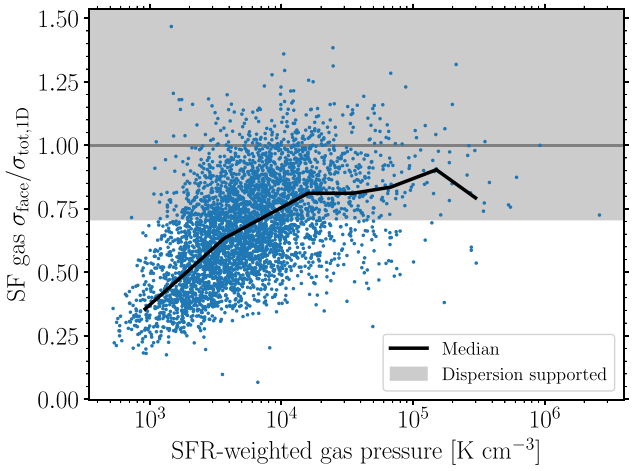

Figure 5. Correlation between dispersion support of star-forming gas and the gas pressure (weighted by the star formation rate of gas particles) for the progenitors of galaxies with stellar masses $2 \times 10^8 < M_*/\,{\rm M}_\odot < 6 \times 10^8$ at $z = 0$. Only galaxies with at least 500 star-forming gas particles are shown. The dispersion support of the star-forming gas is measured as the ratio between the face-on 1D velocity dispersion, $\sigma_{\rm face}$, and the total 1D velocity dispersion, $\sigma_{\rm tot,\,1D}$, after orienting the systems by the spin of the star-forming gas. The dark grey line at $\sigma_{\rm face}/\sigma_{\rm tot,\,1D} = 1$ indicates the velocity dispersion ratio of an isotropic spheroid. The shaded region with $\sigma_{\rm face}/\sigma_{\rm tot,1D} > 1/\sqrt{2}$ indicates where the ratio of kinetic energies is at least 50 per cent, as an approximate estimate for the onset of dispersion-supported dynamics. The dispersion support of star-forming systems correlates with pressure, such that at low gas pressures ($P/k \sim 10^3\,{\rm K\,cm^{-3}}$) they are rotationally supported, while at higher pressures ($P/k \gtrsim 10^4\,{\rm K\,cm^{-3}}$) they are largely dispersion supported.

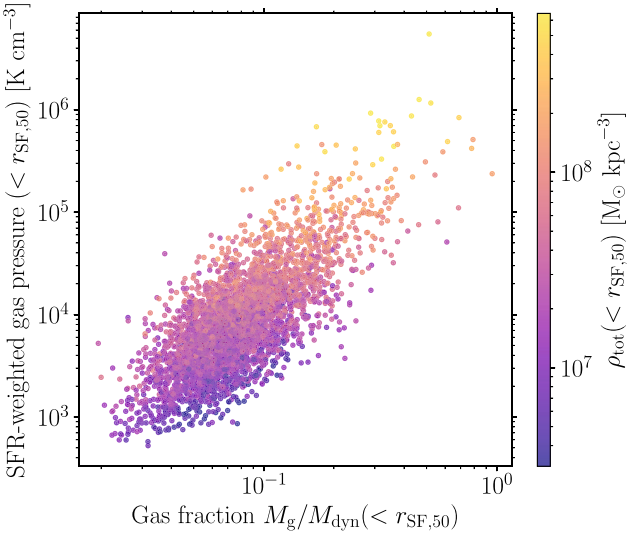

Figure 6. Correlation between gas pressure (weighted by the star formation rate of the gas particles) and gas fraction for the progenitors of galaxies with stellar masses $2 \times 10^8 < M_*/\,{\rm M}_\odot < 6 \times 10^8$ at $z = 0$ (as in Fig. 5). The points for each galaxy are coloured by the total mass density. The galaxy properties are calculated within the radius containing 50 per cent of star formation ($r_{\rm SF,\,50}$) to focus on the main regions of star formation. Higher gas fractions and mass densities both lead to higher pressures for star formation.

disruption of satellites. The figure shows the ratio of the face-on 1D velocity dispersion ($\sigma_{\rm face}$, i.e. the vertical velocity dispersion of the disc in the case of an oblate rotator) to the total 1D velocity dispersion ($\sigma_{\rm tot,1D} = \sigma_{\rm tot,3D}/\sqrt{3}$) as a function of star formation rate-weighted gas pressure. We investigate $\sigma_{\rm face}/\sigma_{\rm tot,\,1D}$, rather than other measures of rotation support (e.g. v/σ), in order to understand how the line-of-sight velocity dispersion (i.e. that used to determine dynamical mass) may be affected in rotating systems. The star formation rate weighting accounts for the likelihood of gas particles being converted to stars depending on pressure in the EAGLE model (Schaye et al. 2015). To orient the systems face on, the spin of the star-forming gas system was also determined by weighting the gas particles by their star formation rate. Only galaxies with ≥500 star-forming gas particles are included in the figure so that the dynamics and spin of the gas are reasonably resolved. At a given pressure, there is relatively large scatter in $\sigma_{\rm face}/\sigma_{\rm tot,\,1D}$, which may be driven by processes such as accretion, mergers, and stellar feedback altering the dynamics of the systems.

Fig. 5 shows that at higher pressures ($P/k \gtrsim 10^4\,{\rm K\,cm^{-3}}$) the star-forming gas systems become mostly dispersion supported ($\sigma_{\rm face}/\sigma_{\rm tot,\,1D} > 1/\sqrt{2}$). At lower pressures, $\sigma_{\rm face}/\sigma_{\rm tot,\,1D}$ decreases with pressure, and the star-forming gas becomes increasingly rotationally supported.[4] Given the expected trend between natal pressure and $S_{\rm M}$, galaxies formed with low natal gas pressures are expected to be rotationally supported systems and host few GCs.

3.4 Origin of gas pressure–kinematics correlation

We now investigate the underlying cause of the relation between gas pressure and dynamics. The rotational support of gas in a galaxy is expected to scale with the gas fraction of the galaxy, $v_{\rm rot}/\sigma \propto 1/f_{\rm gas}$ (e.g. Dekel, Sari & Ceverino 2009b; Genzel et al. 2011). In fact, this has been found previously for simulations of UDG formation, where dispersion-supported galaxies tend to accrete gas earlier, and thus achieve higher gas fractions, than rotation-supported galaxies (Cardona-Barrero et al. 2020). Similarly, since gas pressure is expected to scale with gas surface density (as $P \propto \Sigma_{\rm g}{}^2$, under the assumption of hydrostatic equilibrium; e.g. Schaye 2001; Blitz & Rosolowsky 2004; Krumholz & McKee 2005), we may also expect a correlation between gas pressure and gas fraction in the galaxy.

Fig. 6 shows how the gas pressure scales with the gas fraction for the progenitors of galaxies with $2 \times 10^8 < M_*/\,{\rm M}_\odot < 6 \times 10^8$ at $z = 0$. Only central galaxies with at least 500 star-forming gas particles are included in the figure for consistency with Fig. 5. The gas fractions and SFR-weighted pressure are calculated within the radius containing 50 per cent of star formation ($r_{\rm SF,\,50}$) to focus on the main region of star formation in the galaxies, though similar trends are obtained for other choices in radii (e.g. radii containing 90 per cent of star formation). There is a clear trend of increasing gas pressure with increasing gas fraction in galaxies, though with some scatter at a given gas fraction. However, the contribution of the total mass (rather than just gas mass) to the gas pressure must also be taken into account. In the figure, the points for each galaxy are coloured by the total mass density within $r_{\rm SF,\,50}$. At a given gas fraction, higher mass densities result in higher gas pressures, which drives scatter in the gas fraction–gas pressure correlation. This can be expected to drive scatter in the correlations between gas pressure and kinematics (i.e. Fig. 5), as well as GC abundance and kinematics. Overall, we

[4]Note that there is an implied floor in $\sigma_{\rm face}/\sigma_{\rm tot,\,1D}$. The pressure floor in EAGLE (see Section 2.3) implies a minimum $\sigma_{\rm face} = 13\,{\rm km\,s^{-1}}$, though in practice we often find velocity dispersions below this limit. The galaxies in Fig. 5 have a maximum $\sigma_{\rm tot,1D} \approx 50\,{\rm km\,s^{-1}}$, leading to the minimum ratio $\sigma_{\rm face}/\sigma_{\rm tot,\,1D} \approx 0.25$.

arrive at a coherent picture where the gas fractions in dwarf galaxies as they are forming can result in a correlation between the dynamics of galaxies and their GC system richness.

Of course, the kinematics of galaxies can also be influenced by other processes, such as galaxy mergers or harassment (Moore et al. 1996, 1999). Such processes are expected to result in dynamical heating of the galaxies, which could alter any initial correlation between kinematics and GC system richness. To determine how much effect major mergers may have on the dynamics of galaxies, we search the galaxy-merger trees for significant mergers (those capable of drastically changing the dynamics of the system, i.e. major mergers) which occur late in the formation of the galaxies (such that a new disc dominating the mass of the system is unlikely to form).[5] For all simulated galaxies in the stellar mass range $2 \times 10^8 < M_*/\,\mathrm{M}_\odot < 6 \times 10^8$, we find that only ≈5 per cent of galaxies have major mergers (stellar mass ratio $m_2/m_1 > 0.25$) where the stellar mass of the descendant of the merger is at least 50 per cent of the $z = 0$ stellar mass of the galaxy. Thus, in most cases, late galaxy mergers are unlikely to have played a significant role in setting the stellar dynamics of dwarf galaxies. For GC-rich ($S_\mathrm{M} > 0.4$), dwarf galaxies ≈12 per cent of galaxies have undergone late major mergers, compared to ≈4 per cent for GC-poor ($S_\mathrm{M} \leq 0.4$) dwarf galaxies. Thus, late major mergers are more important in setting the dynamics of GC-rich galaxies, but still in a minority of systems.

In clusters, GC-rich galaxies, which are expected to have earlier infall times (Section 3.2), might be subjected to galaxy harassment over a longer period than GC-poor galaxies. However, we are currently unable to investigate the importance of this effect given the spurious particle heating in the simulation (see Section 2.3).

4 DISCUSSION

4.1 Comparison with observations

As we found in Sections 3.3 and 3.4, galaxies that host few GCs may be rotationally-supported systems as conditions favouring disc formation lead to low-pressure star formation (inefficient GC formation). This is consistent with observations showing that early-type dwarf galaxies have richer GC systems than late-type dwarf galaxies (Georgiev et al. 2010). Therefore, in rotationally supported galaxies observed at low inclinations, the measured velocity dispersion is only representative of the vertical support in the disc, and may significantly underestimate the actual mass of the system (e.g. by a factor 16 for $\sigma_\mathrm{face}/\sigma_\mathrm{tot,\,1D} = 0.25$, given $M_\mathrm{dyn} \propto \sigma^2$). If the GC-poor UDGs in Fig. 2 (from Gannon et al. 2022) also have $\sigma_\mathrm{face}/\sigma_\mathrm{tot,\,1D} \approx 0.25$–0.5, then their dynamical masses would be 4–16 times larger, which would bring them in line with the dynamical masses of both the GC-rich UDGs and predictions from the simulations. Clearly, direct observation of rotation or its absence in such galaxies is needed to test the scenario.

To date, only two UDGs have spatially resolved stellar kinematic profiles: NGC1052-DF2 (Emsellem et al. 2019) and DF44 (van Dokkum et al. 2019b). Both galaxies have rich GC systems (∼3-4 per cent of the galaxy luminosity, van Dokkum et al. 2018b, 2019b) and thus, based on the results of this work, we would not expect them to be rotationally supported galaxies. NGC1052-DF2 appears to have prolate rotation, which may be evidence of a merger,[6] tidal stirring or stripping (Emsellem et al. 2019), rather than oblate rotation that would be expected if it were a disc galaxy.[7] DF44 shows no evidence for rotation ($V/\sigma < 0.12$ van Dokkum et al. 2019b), but has an inferred dynamical mass ($M_\mathrm{dyn} \sim 4 \times 10^9\,\mathrm{M}_\odot$) that is consistent with the simulated galaxies (Fig. 2). On the other hand, H I-rich field UDGs (which have few GCs, Jones et al. 2023) show clear rotation in H I (Leisman et al. 2017; Sengupta et al. 2019; Gault et al. 2021; Shi et al. 2021).

Although no GC-poor UDGs in clusters currently have resolved kinematic profiles, oblate rotating galaxies may be detected statistically by comparing their shapes, as long as the number of galaxies is large enough to sample a range of inclinations. In fact, Lim et al. (2018) found that UDGs in the Coma cluster with lower GC-specific frequencies (S_N) have lower axis ratios (b/a), in agreement with our scenario. Similarly, nucleated dwarf galaxies also have rounder shapes than non-nucleated dwarf galaxies (Ferguson & Sandage 1989; Ryden & Terndrup 1994; Lisker et al. 2007; Venhola et al. 2019; Poulain et al. 2021). Such a correlation would also be expected if the formation of nuclear clusters is related to the formation of GCs (e.g. Sánchez-Janssen et al. 2019; see Neumayer, Seth & Böker 2020 for a review of the formation mechanisms of nuclear clusters).

We test this further in Fig. 7 by comparing the GC system richness (specific frequency or specific mass) with stellar axis ratios for a number of observed dwarf galaxy samples. The top left panel of the figure shows dwarf galaxies from the ACS Virgo Cluster Survey, with GC-specific masses from Peng et al. (2008) and ellipticities from Ferrarese et al. (2006). The top right panel of the figure shows UDGs in the Coma cluster, with specific frequencies ($S_{N,V} = N_\mathrm{GC} 10^{0.4[M_V+15]}$) from Forbes et al. (2020) and axis ratios from Yagi et al. (2016). The bottom left panel of the figure shows UDGs in the Perseus cluster, with specific frequencies ($S_{N,\mathrm{F814W}} = N_\mathrm{GC} 10^{0.4[M_\mathrm{F814W}+15]}$) and axis ratios from Janssens et al. (submitted to MNRAS). The bottom right panel of the figure shows UDGs from the MATLAS survey (mainly field galaxies and galaxy groups), with specific frequencies ($T_N = N_\mathrm{GC}/[M_*/10^9\,\mathrm{M}_\odot]$) and axis ratios from Buzzo et al. (2024). The lower mass/luminosity limits for the three UDG samples are chosen to be approximately similar with a limit $M_* \gtrsim 5 \times 10^7\,\mathrm{M}_\odot$. The ACS Virgo Cluster Survey targets slightly higher mass dwarf galaxies, with a lower limit of $M_* > 3 \times 10^8\,\mathrm{M}_\odot$. We also note that specific frequencies calculated in different photometric bands are not directly comparable (e.g. there is an average factor of ≈2.2 difference between the V and ACS z bands, Peng et al. 2008). Therefore, we compare each galaxy sample separately given the different analysis methods used.

For each galaxy sample, the division between 'GC-rich' and 'GC-poor' galaxies is taken at approximately twice the median specific frequency/mass (as in Section 3.2; grey-dashed lines in each panel of the figure, with the exact values listed in the caption). For both the Virgo and Coma clusters, the differences in axis ratios between GC-rich and GC-poor galaxies are statistically significant ($p < 0.1$)

[5] The discussion here differs from cases where mergers alter the gas dynamics, and subsequent star formation, in the system (e.g. mergers leading to UDG formation through increased spin and size of gas discs, Di Cintio et al. 2019; Wright et al. 2021). In that case, the kinematics and GC richness of the system would largely be set by the subsequent star formation (assuming it dominates the total stellar mass). We focus here on cases where the majority of star formation occurs prior to the merger.

[6] It is possible that prolate rotation could also occur due to high-speed galaxy collisions, though in the simulation of Lee et al. (2021) the resulting galaxy is an oblate rotator.

[7] Interestingly, the GC system of NGC1052-DF2 may have rotation which is perpendicular to the stellar rotation (Lewis, Brewer & Wan 2020). However, in this work, we concentrate on the stellar rotation.

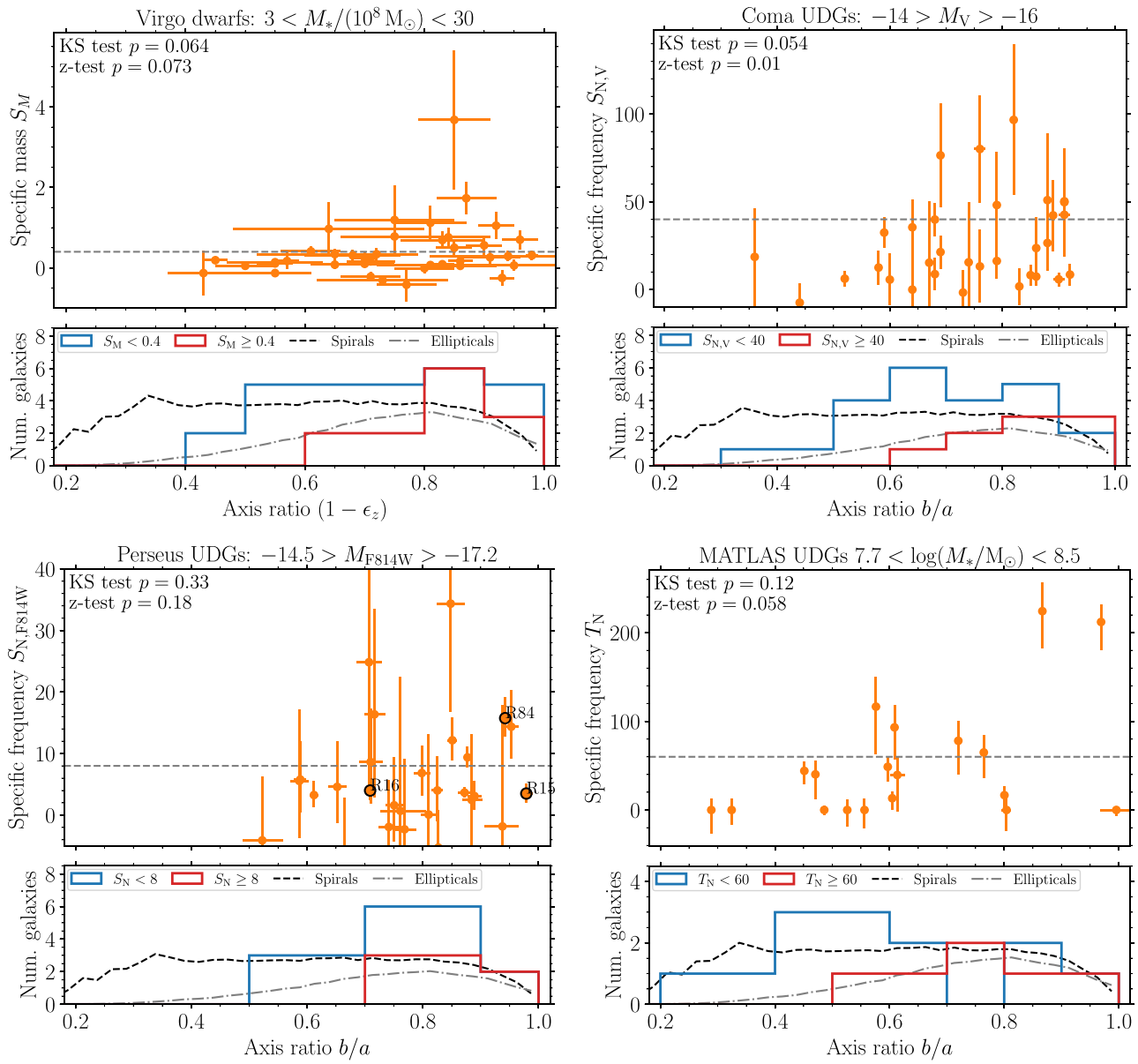

Figure 7. GC system richness (specific frequency or mass) compared with galaxy axis ratios for different observed samples of dwarf galaxies. The top left panels show normal dwarf galaxies from the ACS Virgo Cluster Survey (Ferrarese et al. 2006; Peng et al. 2008). The top-right panels show UDGs in the Coma cluster (Yagi et al. 2016; Forbes et al. 2020). The bottom left panels show UDGs in the Perseus cluster (Janssens et al., submitted to MNRAS) with three UDGs in common with the Gannon et al. (2022) sample highlighted (PUDG R15, R16, and R84). The bottom right panels show UDGs from the MATLAS survey (Buzzo et al. 2024). For each galaxy sample, the bottom subpanel shows the axis ratio histograms for 'GC poor' and 'GC rich' galaxies, where the division is indicated as the grey dashed lines in the main panels at approximately twice the median specific mass/frequency for each sample (top left panel: $S_M = 0.4$; top right panel: $S_{N,V} = 40$; bottom left panel: $S_{N,F814W} = 8$; bottom right panel: $T_N = 60$). For reference, also shown in the subpanels are the axis ratio distributions of bright ($M_r < -19.77$) spiral and elliptical galaxies in the Sloan Digital Sky Survey (Rodríguez & Padilla 2013), with the spiral and elliptical distributions normalized to the number of GC-poor and GC-rich galaxies, respectively. The titles of the main panels show the mass/luminosity limits used for each galaxy sample. To test if the shape distributions for GC-rich and GC-poor galaxies are statistically different, a Kolmogorov–Smirnov and z test were performed for each galaxy sample, with the resulting p-values shown in the main panels. In all samples, the GC-rich galaxies are, on average, rounder than the GC-poor galaxies, which may indicate GC-poor galaxies have flatter intrinsic shapes than GC-rich galaxies (though this difference is not statistically significant for Perseus UDGs).

according to both Kolmogorov–Smirnov and z tests. The Perseus UDGs are not statistically different in either test. For the MATLAS UDGs the GC-rich and GC-poor galaxies are statistically different according to a z test (i.e. statistically different means), but not a Kolmogorov–Smirnov test, which may be a reflection of the smaller sample size. GC-rich galaxies have, on average, higher axis ratios (rounder shapes) than GC-poor galaxies, with an almost complete lack of GC-rich galaxies at $b/a \lesssim 0.6$. Instead, GC-poor galaxies are found to have a wide range of axis ratios, which may be consistent with intrinsically flattened galaxies (oblate or slightly triaxial systems) observed at random inclinations (e.g. see fig. 7 in Sánchez-Janssen et al. 2016). This is found both for UDGs (Coma and MATLAS samples, though not in Perseus) and normal dwarf galaxies in the Virgo cluster.

Comparison of the axis ratio distributions of GC-poor galaxies with spiral galaxies (Rodríguez & Padilla 2013) shows similarly flat distributions, though the cluster dwarf samples (Virgo, Coma, and Perseus) tend to lack very flattened galaxies ($b/a \lesssim 0.3$–0.4) compared to spiral galaxies. This could be a result of formation differences between dwarf galaxies and spirals, galaxy harassment in clusters, or simply selection bias in the samples (e.g. edge-on galaxies are less likely to pass the UDG criteria due to their higher surface brightnesses, He et al. 2019; Cardona-Barrero et al. 2020; Van Nest et al. 2022). In contrast, the GC-rich galaxies have axis ratio distributions which are closer to that of elliptical galaxies (projected axis ratios peaking at $b/a \approx 0.8$, consistent with spheroidal systems with intrinsic 3D axis ratios $C/A \approx 0.6$, Rodríguez & Padilla 2013).

In principle, a trend of galaxies with richer GC systems having rounder shapes could also arise from external environmental processes, rather than galaxy formation processes. For example, GC-rich galaxies, which tend to be found at smaller cluster-centric distances (earlier cluster infall times), may have been more affected by galaxy harassment/tidal heating than GC-poor galaxies. That the trend may also be found for the MATLAS UDG sample (bottom right panel in Fig. 7), where the galaxies are found in much lower density environments (Marleau et al. 2021) than the Virgo, Coma, and Perseus clusters, suggests that galaxy harassment is not the (sole) origin of the correlation.

Previous work has modelled the projected axis ratios of UDGs to determine their intrinsic shapes. Burkert (2017) found that UDGs have prolate shapes. By contrast, both Rong et al. (2020) and Kado-Fong et al. (2021) instead found that UDGs have oblate-triaxial shapes. Rong et al. (2020) suggest the difference in results arises because they considered triaxial models, while Burkert (2017) considered only purely oblate or prolate models. Here, we instead argue that UDGs are not a homogeneous population, but rather a composite of oblate (perhaps slightly triaxial) rotators and dispersion-supported spheroidal galaxies (i.e. the GC-poor and GC-rich galaxies, respectively). This could bias the determination of their intrinsic shape when modelling the axis ratio distributions.

Rong et al. (2020) also found that UDGs in clusters tend to have rounder shapes at smaller cluster-centric distances. This is similarly found for dwarf galaxies in the Fornax cluster (Rong et al. 2019) and by the ACS Virgo Cluster Survey (Ferrarese et al. 2006; Peng et al. 2008). The trend between galaxy shape and cluster-centric distance would agree with the trend we find between GC richness and infall redshift (Fig. 2; i.e. if GC-rich galaxies are typically rounder and earlier-infalling galaxies typically being located at smaller cluster-centric distances, we return to this point in the context of UDGs in the following section). However, again a correlation of shape and cluster-centric radius could also be caused by galaxy harassment/tidal heating. Future simulations, which are not affected by spurious particle heating (Ludlow et al. 2019, see Section 2.3), are needed to disentangle whether harassment or turbulent star formation is more important for setting shapes of cluster dwarf galaxies.

4.2 Formation of UDGs

Given their similar sizes and surface brightnesses (e.g. Leisman et al. 2017), it is natural to consider whether H I-rich field UDGs (or slightly brighter, bluer dwarfs which have since faded, e.g. Román & Trujillo 2017) might be the progenitors of UDGs in clusters which have since had their gas stripped. Based solely on GC numbers (Jones et al. 2023), it is unlikely that present-day H I-rich UDGs could be transformed into GC-rich UDGs. However, it is natural to consider whether H I-rich field UDGs are the progenitors of GC-poor UDGs in clusters. If the dynamical masses (calculated assuming dispersion-supported systems) from Gannon et al. (2022) are correct, to match GC-poor UDGs, the H I-rich UDGs would need to undergo significant dynamical evolution to remove most of their central dark matter mass, and at a much higher level of mass-loss than found in the simulated galaxies. This appears unlikely, as dark matter mass-loss would need to disproportionately affect GC-poor UDGs compared to GC-rich UDGs, given that the latter do agree with simulated galaxies (Fig. 2). Instead, the dark matter halos of H I-rich UDGs and GC-poor cluster UDGs would have to be significantly different initially (e.g. cored dark matter profiles in only cluster galaxies, though cored haloes are less able to survive tidal disruption, Errani et al. 2023; the dark matter profiles of UDGs is further discussed below). GC-poor cluster UDGs might instead form from baryon-dominated field UDGs (Mancera Piña et al. 2019, 2020; Kong et al. 2022; Mancera Piña et al. 2022) which have lost their gas within the cluster (Gannon et al. 2023). Such galaxies are suggested to form due to weak stellar feedback (Mancera Piña et al. 2019, 2020), though this would lead to increased star formation and consumption of gas (e.g. Crain et al. 2015), which appears inconsistent with such gas-rich galaxies. Sellwood & Sanders (2022) also show that such baryon-dominated discs would be unstable, thus requiring an increased dark matter fraction. Reconciling the rotation curves of baryon-dominated UDGs with normal H I-rich galaxies would require their inclinations are systematically overestimated (Karunakaran et al. 2020; Mancera Piña et al. 2022; Sellwood & Sanders 2022). A larger sample of dynamical mass measurements of edge-on, H I-rich UDGs (He et al. 2019), where inclination corrections are small, may help resolve the issue.

Alternatively, as we have discussed in this work, the velocity dispersions of GC-poor cluster UDGs might instead underestimate their mass if they are oblate rotating galaxies observed at low inclinations. This could be due to selection effects, where only oblate galaxies that are (nearly) face-on may be classified as UDGs (He et al. 2019; Cardona-Barrero et al. 2020; Van Nest et al. 2022), which would be particularly important for higher mass UDGs (i.e. typical spectroscopic targets with $M_* \gtrsim 10^8$ M$_\odot$) due to their higher surface brightnesses. In this case, H I-rich UDGs (or higher redshift analogues) could be the progenitors of GC-poor cluster UDGs. GC-rich UDGs may instead differ due to formation biases (early halo and star formation) introduced by early infall and subsequent quenching within groups/clusters. Such an origin was previously advocated by Carleton et al. (2021), who also suggested that the large sizes of cluster UDGs may be due to tidal heating (see also Yozin & Bekki 2015; Safarzadeh & Scannapieco 2017; Ogiya 2018; Carleton et al. 2019; Sales et al. 2020; Tremmel et al. 2020). This might imply that the large sizes of GC-rich and GC-poor UDGs occur (on average) through different processes (echoing previous suggestions of different formation processes for GC-rich and GC-poor UDGs, Forbes et al. 2020). For example, early cluster infall for GC-rich galaxies (Section 3.2) may lead to enhanced tidal heating, while for GC-poor and HI-rich UDGs the large sizes could largely be due to internal galaxy formation processes (e.g. formation in low-concentration or high-spin haloes leading to lower density star formation, Amorisco & Loeb 2016; Leisman et al. 2017; Shi et al. 2021; Benavides et al. 2023; or increase spin and size of gaseous discs due to mergers, Di Cintio et al. 2019; Wright et al. 2021). Indeed, some works find that a combination of formation paths are necessary to reproduce UDG numbers in groups and clusters (e.g. Jiang et al. 2019; Sales et al. 2020; Benavides et al. 2023). Interestingly, based on their phase-space locations, cluster UDGs found in the 'ancient infall' region (small cluster-centric distances and low relative velocities, with infall times greater than 6.45 Gyr ago, or $z > 0.7$, see Rhee

et al. 2017) tend to have lower GC numbers than those in other regions of phase space (Forbes et al. 2023). If GC-rich UDGs form through tidal heating, this appears at odds with the expectation that tidal heating would be more important for earlier-infalling galaxies, though we note that GC-specific frequency of UDGs does decrease with increasing cluster-centric radius in the Coma cluster (Lim et al. 2018). Further study is clearly needed, but it is possible that tidal heating of ancient infall UDGs might become 'too efficient' in this region, instead leading to compact galaxies from tidal stripping, complete disruption or the formation of ultracompact dwarf galaxies from nucleated UDGs (Janssens et al. 2019; Wang et al. 2023). In this interpretation, GC-poor UDGs in the ancient infall region of phase-space might instead have more recent infall times (Rhee et al. 2017 find that nearly 50 per cent of galaxies in the 'ancient infall' region of phase-space actually have later infall redshifts).

The enclosed dynamical masses of galaxies are, of course, also dependent on their dark matter profiles. Many works suggest that UDGs reside within cored, rather than cuspy (i.e. an NFW profile, Navarro, Frenk & White 1996b, 1997), dark matter haloes (e.g. Di Cintio et al. 2017; Carleton et al. 2019; Martin et al. 2019; van Dokkum et al. 2019b), where the cores are generally thought to form through stellar feedback processes (e.g. Navarro et al. 1996a; Read & Gilmore 2005; Governato et al. 2010; Macciò et al. 2012; Pontzen & Governato 2012). Such a feedback-driven expansion is also potentially more efficient in GC-rich galaxies (e.g. Trujillo-Gomez et al. 2021; Trujillo-Gomez et al. 2022). Galaxies in the EAGLE model (and thus also in this work) do not form dark matter cores unless the star formation density threshold is significantly increased (Benítez-Llambay et al. 2019). However, EAGLE galaxies may appear cored in mock observations (Oman et al. 2019) and models with cusps may better explain the diversity of galaxy rotation curves than those with cores (Roper et al. 2023).

The measured kinematic profiles of UDGs are contradictory: some UDGs are consistent with core profiles (van Dokkum et al. 2019b; Gannon et al. 2022, 2023), and others are consistent with NFW haloes (Leisman et al. 2017; Sengupta et al. 2019; Shi et al. 2021, though see also Brook et al. 2021 who suggest a shallower inner profile slope in the case of AGC 242019). In general, the dynamics of cluster and field galaxies are determined using different methods (using stellar and gas kinematics, respectively) and thus have different sources of uncertainties and systematics. In the case of gas rotation profiles, many types of perturbations can affect their dynamics, leading to rotation profiles that do not match the true circular velocity profiles (Downing & Oman 2023) and cuspy halo profiles appearing to be cored (Hayashi & Navarro 2006; Pineda et al. 2017; Oman et al. 2019; Roper et al. 2023). From their stellar dynamics, the cluster UDGs tend to favour cored profiles (van Dokkum et al. 2019b; Gannon et al. 2022, 2023) when assuming standard mass–concentration relations for cuspy haloes. However, as we find in Fig. 2, inferring the initial dark matter halo profile for satellite galaxies in clusters from their dynamical masses may be difficult, as most galaxies (except for very recent accretion) have undergone significant tidal stripping of their dark matter halo. In this case, cored dark matter profiles could be inferred from lower-than-expected dynamical masses, despite having cuspy profiles (cusps are retained during tidal stripping, Kazantzidis et al. 2004).

In Fig. 8, we compare the stellar and dark matter mass profiles for one of the simulated galaxies in Fig. 3 that have undergone the most tidal stripping (i.e. have the highest $M_*/M_{\rm dyn}$; the result for the other galaxy is similar). At $z = 2.48$, prior to becoming a satellite, the dark matter halo of the galaxy initially follows an NFW profile (solid orange line in top panel), though the smaller virial

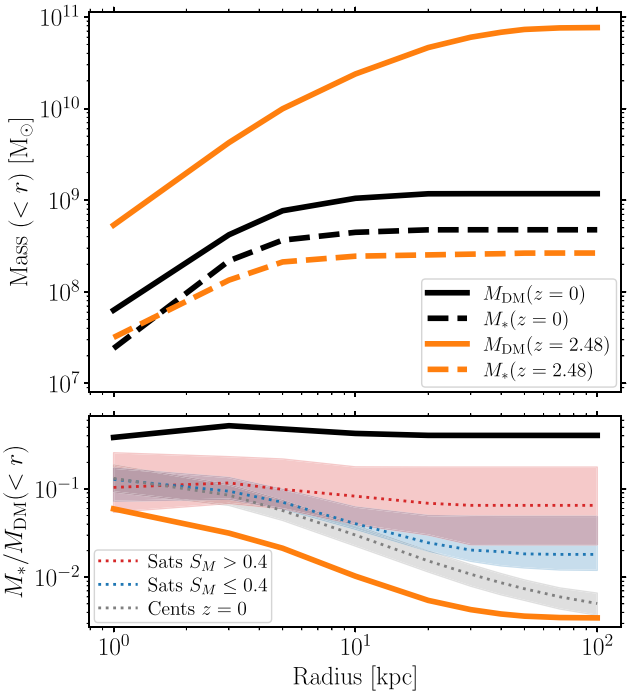

Figure 8. Comparison of the initial (redshift prior to becoming a satellite, thick orange lines) and $z = 0$ (thick black lines) enclosed mass profiles for a galaxy which has undergone strong tidal stripping of the dark matter halo (i.e. highest $M_*/M_{\rm dyn}$ in Fig. 3). In the upper panel, solid lines show the dark matter mass profiles, while dashed lines show the stellar mass profiles. The lower panel shows the stellar-to-dark matter mass profiles at each redshift. The mass profile is shown at larger radii than the gravitational softening length (0.35 kpc). Unlike the initial profile, at $z = 0$, the stellar-to-dark matter mass ratio is roughly constant (≈0.5). For comparison, the dotted grey, blue, and red lines show the median mass ratio at each radius for $z = 0$ central galaxies and GC-poor ($S_{\rm M} \leq 0.4$) and GC-rich ($S_{\rm M} > 0.4$) satellite galaxies in groups/clusters (i.e. those in Fig. 2), respectively, with shaded regions showing the 16$^{\rm th}$ to 84$^{\rm th}$ percentiles for each population. As found in Figs 2 and 3, from GC-poor to GC-rich satellite galaxies there is an increasing trend of dark matter mass-loss compared to central galaxies.

radius of the high-redshift halo compared to typical $z = 0$ haloes (see also Section 3.1) results in a lower stellar-to-dark matter mass ratio at small radii (bottom panel, orange line compared to grey-dotted line). However, we find that the $z = 0$ dark matter profile of the galaxy appears approximately as scaled version of the stellar mass profile (the enclosed stellar mass-to-dark matter mass ratio is nearly constant with radius) rather than an NFW profile (which might be expected for tidally limited galaxies, Errani et al. 2022). Thus, galaxies in such highly stripped haloes will have very different mass profiles compared to galaxies residing in typical isolated dark matter haloes at $z = 0$ (grey line in the figure), which should be taken into account when fitting dynamical mass profiles to observed galaxies. In the median, the differences in enclosed stellar-to-dark matter ratios compared to $z = 0$ central galaxies increases from GC-poor satellites (blue-dotted line) to GC-rich satellites (red-dotted line) at radii $\gtrsim 5$ kpc due to increased tidal stripping of the dark matter haloes.

5 SUMMARY

In this work, we used simulations of galaxies and their GC systems from the E-MOSAICS project to investigate possible origins of

the observed correlation between stellar velocity dispersion (or dynamical mass) and GC system richness in UDGs (Gannon et al. 2022). We found that the simulations in fact predict the opposite trend, with GC-rich galaxies having lower enclosed masses than GC-poor galaxies (Section 3.2). This occurs due to the earlier infall times ($z_{\rm infall} \gtrsim 1$) of GC-rich galaxies in galaxy groups/clusters, resulting in increased tidal stripping of their dark matter haloes compared to GC-poor galaxies. However, the enclosed masses for the simulated GC-rich galaxies agree well with the dynamical masses of observed GC-rich UDGs. Therefore, we find that GC-rich UDGs are consistent with being a population of early-infalling galaxies (see also Carleton et al. 2021) which have subsequently undergone tidal stripping of much of their dark matter haloes (a process that could also result in tidal heating to explain the large sizes of UDGs, e.g. Yozin & Bekki 2015; Safarzadeh & Scannapieco 2017; Ogiya 2018; Carleton et al. 2019; Sales et al. 2020; though this may be at odds with the phase-space locations of GC-rich UDGs in clusters, Forbes et al. 2023, see Section 4.2 for further discussion).

In contrast, the simulated GC-poor galaxies have enclosed masses that are generally inconsistent with those found for GC-poor cluster UDGs from their stellar velocity dispersions (Gannon et al. 2022). However, the enclosed masses of isolated and late infalling ($z_{\rm infall} \lesssim 0.3$) simulated galaxies do agree well with the dynamical masses of H I-rich field galaxies and edge-on UDGs (Lelli et al. 2016; He et al. 2019). If tidal stripping of the dark matter haloes were to explain the lower inferred dynamical masses of GC-poor cluster UDGs, it would require GC-poor galaxies to have earlier infall times or be preferentially more affected than GC-rich galaxies, which we consider to be unlikely. Instead, we considered whether the kinematics of GC-poor galaxies are systematically different from those of GC-rich galaxies. If GC-poor UDGs are rotating systems observed nearly face on, such that their velocity dispersion is only representative of the vertical disc support, their velocity dispersions would underestimate the total mass in the system. This may be particularly important for higher mass UDGs (i.e. typical spectroscopic targets), as edge-on systems may not be classified as UDGs due to their higher surface brightnesses (He et al. 2019; Van Nest et al. 2022).

In this work, we used the simulations to show that galactic conditions for star formation could result in an anticorrelation between the rotational support of galaxies and their GC system richness (Sections 3.3 and 3.4). Galaxies with higher gas fractions are turbulent systems with low rotational support (e.g. Dekel et al. 2009a; Genzel et al. 2011), but typically have high gas pressures (Fig. 6), leading to efficient GC formation (Fig. 4, Kruijssen 2012; Pfeffer et al. 2018). Conversely, lower gas fractions lead to more rotational support and lower gas pressures, resulting in less efficient GC formation. Though we focus on a small galaxy mass range in this work ($2 \times 10^8 < M_*/\,{\rm M}_\odot < 6 \times 10^8\,{\rm M}_\odot$), such processes are not unique to any mass range, and may therefore explain why early-type galaxies at all masses typically have richer GC systems than late-type galaxies (Georgiev et al. 2010).

Though there are currently no GC-poor UDGs in clusters with resolved stellar kinematic profiles to test for rotation, oblate rotating galaxies would be expected to have a different distribution of shapes (projected axis ratios, b/a) to dispersion-supported spheroidal galaxies. For UDGs in the Coma cluster, galaxies with lower GC-specific frequencies are indeed found to have lower axis ratios than those with high specific frequencies (Lim et al. 2018), which may indicate that they are (nearly) oblate systems. We expanded this comparison to include Virgo cluster dwarf galaxies, UDGs in the Perseus cluster, and UDGs from the MATLAS survey (Section 4.1). In all observed galaxy samples, GC-rich galaxies are found to have relatively round shapes ($b/a \gtrsim 0.6$) that are similar to those of elliptical galaxies, while GC-poor galaxies typically have a wider range of shapes ($b/a \approx 0.3$–1) that are similar to spiral galaxies. No very flattened galaxies ($b/a < 0.5$) were found to be GC-rich systems.

Therefore, current observations support a scenario where GC-poor galaxies are (on average) discy, rotating systems. This may explain the low observed stellar velocity dispersions of GC-poor UDGs in the Perseus cluster (Gannon et al. 2022), implying underestimated dynamical masses if they are near face-on discs, and reconciling their masses with those of simulated galaxies (Section 3.2). This would also make GC-poor UDGs natural analogues of H I-rich field UDGs, which have since lost their gas after entering the group/cluster environment. Future observations should test directly for our predicted stellar rotation within GC-poor UDGs, as well as further dynamical mass measurements of highly flattened UDGs, where inclination corrections are small.

ACKNOWLEDGEMENTS

This work was supported by the Australian government through the Australian Research Council's Discovery Projects funding scheme (DP220101863) and the Australian Research Council Centre of Excellence for All Sky Astrophysics in 3 Dimensions (ASTRO 3D), through project number CE170100013. JMDK gratefully acknowledges funding from the European Research Council (ERC) under the European Union's Horizon 2020 research and innovation programme via the ERC Starting Grant MUSTANG (grant agreement number 714907). COOL Research DAO is a Decentralized Autonomous Organization supporting research in astrophysics aimed at uncovering our cosmic origins. AJR was supported by National Science Foundation grant AST-2308390. Support for Program number HST-GO-15235 was provided through a grant from the STScI under NASA contract NAS5-26555. This work used the DiRAC Data Centric system at Durham University, operated by the Institute for Computational Cosmology on behalf of the STFC DiRAC HPC Facility (www.dirac.ac.uk). This equipment was funded by BIS National E-infrastructure capital grant ST/K00042X/1, STFC capital grants ST/H008519/1 and ST/K00087X/1, STFC DiRAC Operations grant ST/K003267/1 and Durham University. DiRAC is part of the National E-Infrastructure. The work also made use of high performance computing facilities at Liverpool John Moores University, partly funded by the Royal Society and LJMU's Faculty of Engineering and Technology.

DATA AVAILABILITY

The data underlying this paper will be shared on reasonable request to the corresponding author.

REFERENCES

Aguerri J. A. L., Girardi M., Agulli I., Negri A., Dalla Vecchia C., Domínguez Palmero L., 2020, MNRAS, 494, 1681
Amorisco N. C., Loeb A., 2016, MNRAS, 459, L51
Amorisco N. C., Monachesi A., Agnello A., White S. D. M., 2018, MNRAS, 475, 4235
Baldry I. K. et al., 2012, MNRAS, 421, 621
Bastian N., 2008, MNRAS, 390, 759
Bastian N., Pfeffer J., Kruijssen J. M. D., Crain R. A., Trujillo-Gomez S., Reina-Campos M., 2020, MNRAS, 498, 1050
Beasley M. A., Trujillo I., 2016, ApJ, 830, 23

Beasley M. A., Romanowsky A. J., Pota V., Navarro I. M., Martinez Delgado D., Neyer F., Deich A. L., 2016, ApJ, 819, L20
Benavides J. A., Sales L. V., Abadi M. G., Marinacci F., Vogelsberger M., Hernquist L., 2023, MNRAS, 522, 1033
Benítez-Llambay A., Navarro J. F., Frenk C. S., Ludlow A. D., 2018, MNRAS, 473, 1019
Benítez-Llambay A., Frenk C. S., Ludlow A. D., Navarro J. F., 2019, MNRAS, 488, 2387
Bignone L. A., Pedrosa S. E., Trayford J. W., Tissera P. B., Pellizza L. J., 2020, MNRAS, 491, 3624
Blakeslee J. P., 1999, AJ, 118, 1506
Blakeslee J. P., Tonry J. L., Metzger M. R., 1997, AJ, 114, 482
Blitz L., Rosolowsky E., 2004, ApJ, 612, L29
Booth C. M., Schaye J., 2009, MNRAS, 398, 53
Bournaud F. et al., 2007, Science, 316, 1166
Bouwens R. J., Illingworth G. D., van Dokkum P. G., Ribeiro B., Oesch P. A., Stefanon M., 2021, AJ, 162, 255
Brook C. B., Di Cintio A., Macciò A. V., Blank M., 2021, ApJ, 919, L1
Bullock J. S., Kolatt T. S., Sigad Y., Somerville R. S., Kravtsov A. V., Klypin A. A., Primack J. R., Dekel A., 2001, MNRAS, 321, 559
Burkert A., 2017, ApJ, 838, 93
Burkert A., Forbes D. A., 2020, AJ, 159, 56
Buzzo M. L. et al., 2024, MNRAS, 529, 3210, https://doi.org/10.1093/mnras/stae564
Cardona-Barrero S., Di Cintio A., Brook C. B. A., Ruiz-Lara T., Beasley M. A., Falcón-Barroso J., Macciò A. V., 2020, MNRAS, 497, 4282
Carleton T., Errani R., Cooper M., Kaplinghat M., Peñarrubia J., Guo Y., 2019, MNRAS, 485, 382
Carleton T., Guo Y., Munshi F., Tremmel M., Wright A., 2021, MNRAS, 502, 398
Chan T. K., Kereš D., Wetzel A., Hopkins P. F., Faucher-Giguère C. A., El-Badry K., Garrison-Kimmel S., Boylan-Kolchin M., 2018, MNRAS, 478, 906
Cole S., Lacey C., 1996, MNRAS, 281, 716
Colín P., Klypin A. A., Kravtsov A. V., 2000, ApJ, 539, 561
Crain R. A. et al., 2015, MNRAS, 450, 1937
Crain R. A. et al., 2017, MNRAS, 464, 4204
Danieli S., van Dokkum P., Conroy C., Abraham R., Romanowsky A. J., 2019, ApJ, 874, L12
Danieli S. et al., 2022, ApJ, 927, L28
Davis M., Efstathiou G., Frenk C. S., White S. D. M., 1985, ApJ, 292, 371
Dekel A. et al., 2009a, Nature, 457, 451
Dekel A., Sari R., Ceverino D., 2009b, ApJ, 703, 785
Di Cintio A., Brook C. B., Dutton A. A., Macciò A. V., Obreja A., Dekel A., 2017, MNRAS, 466, L1
Di Cintio A., Brook C. B., Macciò A. V., Dutton A. A., Cardona-Barrero S., 2019, MNRAS, 486, 2535
Dolag K., Borgani S., Murante G., Springel V., 2009, MNRAS, 399, 497
Doppel J. E., Sales L. V., Navarro J. F., Abadi M. G., Peng E. W., Toloba E., Ramos-Almendares F., 2021, MNRAS, 502, 1661
Downing E. R., Oman K. A., 2023, MNRAS, 522, 3318
Emsellem E. et al., 2019, A&A, 625, A76
Errani R., Navarro J. F., Ibata R., Peñarrubia J., 2022, MNRAS, 511, 6001
Errani R., Navarro J. F., Peñarrubia J., Famaey B., Ibata R., 2023, MNRAS, 519, 384
Ferguson H. C., Sandage A., 1989, ApJ, 346, L53
Ferrarese L. et al., 2006, ApJS, 164, 334
Forbes D. A., Gannon J., 2024, MNRAS, 528, 608
Forbes D. A., Alabi A., Romanowsky A. J., Brodie J. P., Arimoto N., 2020, MNRAS, 492, 4874
Forbes D. A., Gannon J. S., Romanowsky A. J., Alabi A., Brodie J. P., Couch W. J., Ferré-Mateu A., 2021, MNRAS, 500, 1279
Forbes D. A. et al., 2023, MNRAS, 525, L93
Furlong M. et al., 2015, MNRAS, 450, 4486
Furlong M. et al., 2017, MNRAS, 465, 722
Gannon J. S., Forbes D. A., Romanowsky A. J., Ferré-Mateu A., Couch W. J., Brodie J. P., 2020, MNRAS, 495, 2582
Gannon J. S. et al., 2021, MNRAS, 502, 3144
Gannon J. S. et al., 2022, MNRAS, 510, 946
Gannon J. S., Forbes D. A., Brodie J. P., Romanowsky A. J., Couch W. J., Ferré-Mateu A., 2023, MNRAS, 518, 3653
Gault L. et al., 2021, ApJ, 909, 19
Genzel R. et al., 2011, ApJ, 733, 101
Georgiev I. Y., Puzia T. H., Goudfrooij P., Hilker M., 2010, MNRAS, 406, 1967
Gnedin O. Y., Hernquist L., Ostriker J. P., 1999, ApJ, 514, 109
Governato F. et al., 2010, Nature, 463, 203
Harris W. E., Harris G. L. H., Alessi M., 2013, ApJ, 772, 82
Harris W. E., Blakeslee J. P., Harris G. L. H., 2017, ApJ, 836, 67
Hayashi E., Navarro J. F., 2006, MNRAS, 373, 1117
He M., Wu H., Du W., Wicker J., Zhao P., Lei F., Liu J., 2019, ApJ, 880, 30
Horta D., Hughes M. E., Pfeffer J. L., Bastian N., Kruijssen J. M. D., Reina-Campos M., Crain R. A., 2021, MNRAS, 500, 4768
Hughes M. E., Pfeffer J. L., Bastian N., Martig M., Kruijssen J. M. D., Crain R. A., Reina-Campos M., Trujillo-Gomez S., 2022, MNRAS, 510, 6190
Hunter D. A., Elmegreen B. G., 2006, ApJS, 162, 49
Jackson R. A. et al., 2021, MNRAS, 502, 1785
Janssens S., Abraham R., Brodie J., Forbes D., Romanowsky A. J., van Dokkum P., 2017, ApJ, 839, L17
Janssens S. R., Abraham R., Brodie J., Forbes D. A., Romanowsky A. J., 2019, ApJ, 887, 92
Jiang L., Helly J. C., Cole S., Frenk C. S., 2014, MNRAS, 440, 2115
Jiang F., Dekel A., Freundlich J., Romanowsky A. J., Dutton A. A., Macciò A. V., Di Cintio A., 2019, MNRAS, 487, 5272
Jing Y., Wang C., Li R., Liao S., Wang J., Guo Q., Gao L., 2019, MNRAS, 488, 3298
Jones M. G. et al., 2023, ApJ, 942, L5
Jordán A. et al., 2007, ApJS, 171, 101
Kado-Fong E. et al., 2021, ApJ, 920, 72
Karunakaran A., Spekkens K., Zaritsky D., Donnerstein R. L., Kadowaki J., Dey A., 2020, ApJ, 902, 39
Kazantzidis S., Mayer L., Mastropietro C., Diemand J., Stadel J., Moore B., 2004, ApJ, 608, 663
Keim M. A. et al., 2022, ApJ, 935, 160
Kennicutt R. C., Jr, 1998, ApJ, 498, 541
Kong D., Kaplinghat M., Yu H.-B., Fraternali F., Mancera Piña P. E., 2022, ApJ, 936, 166
Kruijssen J. M. D., 2012, MNRAS, 426, 3008
Kruijssen J. M. D., Pelupessy F. I., Lamers H. J. G. L. M., Portegies Zwart S. F., Icke V., 2011, MNRAS, 414, 1339
Kruijssen J. M. D., Pfeffer J. L., Crain R. A., Bastian N., 2019a, MNRAS, 486, 3134
Kruijssen J. M. D., Pfeffer J. L., Reina-Campos M., Crain R. A., Bastian N., 2019b, MNRAS, 486, 3180
Kruijssen J. M. D. et al., 2020, MNRAS, 498, 2472
Krumholz M. R., McKee C. F., 2005, ApJ, 630, 250
La Marca A. et al., 2022, A&A, 665, A105
Lagos C. d. P. et al., 2015, MNRAS, 452, 3815
Lamers H. J. G. L. M., Gieles M., Bastian N., Baumgardt H., Kharchenko N. V., Portegies Zwart S., 2005, A&A, 441, 117
Lee J., Shin E.-j., Kim J.-h., 2021, ApJ, 917, L15
Leisman L. et al., 2017, ApJ, 842, 133
Lelli F. et al., 2015, A&A, 584, A113
Lelli F., McGaugh S. S., Schombert J. M., 2016, AJ, 152, 157
Lewis G. F., Brewer B. J., Wan Z., 2020, MNRAS, 491, L1
Li C., White S. D. M., 2009, MNRAS, 398, 2177
Lim S., Peng E. W., Côté P., Sales L. V., den Brok M., Blakeslee J. P., Guhathakurta P., 2018, ApJ, 862, 82
Lim S. et al., 2020, ApJ, 899, 69
Lisker T., Grebel E. K., Binggeli B., Glatt K., 2007, ApJ, 660, 1186
Ludlow A. D., Schaye J., Schaller M., Richings J., 2019, MNRAS, 488, L123
Ludlow A. D., Fall S. M., Schaye J., Obreschkow D., 2021, MNRAS, 508, 5114
Ludlow A. D., Fall S. M., Wilkinson M. J., Schaye J., Obreschkow D., 2023, MNRAS, 525, 5614
McConnachie A. W., 2012, AJ, 144, 4

McAlpine S. et al., 2016, Astron. Comput., 15, 72
Macciò A. V., Stinson G., Brook C. B., Wadsley J., Couchman H. M. P., Shen S., Gibson B. K., Quinn T., 2012, ApJ, 744, L9
Macciò A. V., Prats D. H., Dixon K. L., Buck T., Waterval S., Arora N., Courteau S., Kang X., 2021, MNRAS, 501, 693
Mancera Piña P. E. et al., 2019, ApJ, 883, L33
Mancera Piña P. E. et al., 2020, MNRAS, 495, 3636
Mancera Piña P. E., Fraternali F., Oosterloo T., Adams E. A. K., Oman K. A., Leisman L., 2022, MNRAS, 512, 3230
Marleau F. R. et al., 2021, A&A, 654, A105
Martín-Navarro I. et al., 2019, MNRAS, 484, 3425
Martin G. et al., 2019, MNRAS, 485, 796
Martínez-Delgado D. et al., 2016, AJ, 151, 96
Misgeld I., Hilker M., 2011, MNRAS, 414, 3699
Mistani P. A. et al., 2016, MNRAS, 455, 2323
Montes M., Infante-Sainz R., Madrigal-Aguado A., Román J., Monelli M., Borlaff A. S., Trujillo I., 2020, ApJ, 904, 114
Moore B., Katz N., Lake G., Dressler A., Oemler A., 1996, Nature, 379, 613
Moore B., Lake G., Quinn T., Stadel J., 1999, MNRAS, 304, 465
Moreno J. et al., 2022, Nat. Astron., 6, 496
Müller O. et al., 2020, A&A, 640, A106
Navarro J. F., Eke V. R., Frenk C. S., 1996a, MNRAS, 283, L72
Navarro J. F., Frenk C. S., White S. D. M., 1996b, ApJ, 462, 563
Navarro J. F., Frenk C. S., White S. D. M., 1997, ApJ, 490, 493
Neumayer N., Seth A., Böker T., 2020, A&A Rev., 28, 4
Norris M. A. et al., 2014, MNRAS, 443, 1151
Ogiya G., 2018, MNRAS, 480, L106
Ogiya G., van den Bosch F. C., Burkert A., 2022, MNRAS, 510, 2724
Oman K. A., Marasco A., Navarro J. F., Frenk C. S., Schaye J., Benítez-Llambay A., 2019, MNRAS, 482, 821
Peng E. W. et al., 2008, ApJ, 681, 197
Pfeffer J., Kruijssen J. M. D., Crain R. A., Bastian N., 2018, MNRAS, 475, 4309
Pfeffer J., Bastian N., Crain R. A., Kruijssen J. M. D., Hughes M. E., Reina-Campos M., 2019a, MNRAS, 487, 4550
Pfeffer J., Bastian N., Kruijssen J. M. D., Reina-Campos M., Crain R. A., Usher C., 2019b, MNRAS, 490, 1714
Pfeffer J., Cavanagh M. K., Bekki K., Couch W. J., Drinkwater M. J., Forbes D. A., Koribalski B. S., 2023a, MNRAS, 518, 5260
Pfeffer J., Kruijssen J. M. D., Bastian N., Crain R. A., Trujillo-Gomez S., 2023b, MNRAS, 519, 5384
Pineda J. C. B., Hayward C. C., Springel V., Mendes de Oliveira C., 2017, MNRAS, 466, 63
Planck Collaboration XVI, 2014, A&A, 571, A16
Pontzen A., Governato F., 2012, MNRAS, 421, 3464
Poulain M. et al., 2021, MNRAS, 506, 5494
Poulain M. et al., 2022, A&A, 659, A14
Prieto J. L., Gnedin O. Y., 2008, ApJ, 689, 919
Qu Y. et al., 2017, MNRAS, 464, 1659
Read J. I., Gilmore G., 2005, MNRAS, 356, 107
Reina-Campos M., Kruijssen J. M. D., 2017, MNRAS, 469, 1282
Reina-Campos M., Trujillo-Gomez S., Deason A. J., Kruijssen J. M. D., Pfeffer J. L., Crain R. A., Bastian N., Hughes M. E., 2022, MNRAS, 513, 3925
Rhee J., Smith R., Choi H., Yi S. K., Jaffé Y., Candlish G., Sánchez-Jánssen R., 2017, ApJ, 843, 128
Rodríguez S., Padilla N. D., 2013, MNRAS, 434, 2153
Román J., Trujillo I., 2017, MNRAS, 468, 4039
Román J., Jones M. G., Montes M., Verdes-Montenegro L., Garrido J., Sánchez S., 2021, A&A, 649, L14
Rong Y. et al., 2019, ApJ, 883, 56
Rong Y. et al., 2020, ApJ, 899, 78
Roper F. A., Oman K. A., Frenk C. S., Benítez-Llambay A., Navarro J. F., Santos-Santos I. M. E., 2023, MNRAS, 521, 1316
Rosas-Guevara Y. M. et al., 2015, MNRAS, 454, 1038
Ryden B. S., Terndrup D. M., 1994, ApJ, 425, 43
Safarzadeh M., Scannapieco E., 2017, ApJ, 850, 99
Sales L. V., Navarro J. F., Peñafiel L., Peng E. W., Lim S., Hernquist L., 2020, MNRAS, 494, 1848
Sales L. V., Wetzel A., Fattahi A., 2022, Nat. Astron., 6, 897
Sánchez-Janssen R. et al., 2016, ApJ, 820, 69
Sánchez-Janssen R. et al., 2019, ApJ, 878, 18
Schaye J., 2001, ApJ, 559, 507
Schaye J., Dalla Vecchia C., 2008, MNRAS, 383, 1210
Schaye J. et al., 2015, MNRAS, 446, 521
Schechter P., 1976, ApJ, 203, 297
Sellwood J. A., Sanders R. H., 2022, MNRAS, 514, 4008
Sengupta C., Scott T. C., Chung A., Wong O. I., 2019, MNRAS, 488, 3222
Shen Z. et al., 2021, ApJ, 914, L12
Shen Z., van Dokkum P., Danieli S., 2023, ApJ, 957, 6
Shi Y., Zhang Z.-Y., Wang J., Chen J., Gu Q., Yu X., Li S., 2021, ApJ, 909, 20
Shin E.-j., Jung M., Kwon G., Kim J.-h., Lee J., Jo Y., Oh B. K., 2020, ApJ, 899, 25
Silk J., 2019, MNRAS, 488, L24
Spitler L. R., Forbes D. A., 2009, MNRAS, 392, L1
Springel V., 2005, MNRAS, 364, 1105
Springel V., White S. D. M., Tormen G., Kauffmann G., 2001, MNRAS, 328, 726
Toloba E. et al., 2018, ApJ, 856, L31
Toloba E. et al., 2023, ApJ, 951, 77
Trayford J. W. et al., 2017, MNRAS, 470, 771
Tremmel M., Wright A. C., Brooks A. M., Munshi F., Nagai D., Quinn T. R., 2020, MNRAS, 497, 2786
Trujillo-Gomez S., Kruijssen J. M. D., Keller B. W., Reina-Campos M., 2021, MNRAS, 506, 4841
Trujillo-Gomez S., Kruijssen J. M. D., Reina-Campos M., 2022, MNRAS, 510, 3356
Usher C., Pfeffer J., Bastian N., Kruijssen J. M. D., Crain R. A., Reina-Campos M., 2018, MNRAS, 480, 3279
van der Burg R. F. J., Muzzin A., Hoekstra H., 2016, A&A, 590, A20
van Dokkum P. G., Abraham R., Merritt A., Zhang J., Geha M., Conroy C., 2015a, ApJ, 798, L45
van Dokkum P. G. et al., 2015b, ApJ, 804, L26
van Dokkum P. et al., 2016, ApJ, 828, L6
van Dokkum P. et al., 2017, ApJ, 844, L11
van Dokkum P. et al., 2018a, Nature, 555, 629
van Dokkum P. et al., 2018b, ApJ, 856, L30
van Dokkum P., Danieli S., Abraham R., Conroy C., Romanowsky A. J., 2019a, ApJ, 874, L5
van Dokkum P. et al., 2019b, ApJ, 880, 91
van Dokkum P. et al., 2022, Nature, 605, 435
Van Nest J. D., Munshi F., Wright A. C., Tremmel M., Brooks A. M., Nagai D., Quinn T., 2022, ApJ, 926, 92
Venhola A. et al., 2019, A&A, 625, A143
Wiersma R. P. C., Schaye J., Smith B. D., 2009a, MNRAS, 393, 99
Wang K. et al., 2023, Nature, 623, 296
Wiersma R. P. C., Schaye J., Theuns T., Dalla Vecchia C., Tornatore L., 2009b, MNRAS, 399, 574
Wilkinson M. J., Ludlow A. D., Lagos C. d. P., Fall S. M., Schaye J., Obreschkow D., 2023, MNRAS, 519, 5942
Wolf J., Martinez G. D., Bullock J. S., Kaplinghat M., Geha M., Muñoz R. R., Simon J. D., Avedo F. F., 2010, MNRAS, 406, 1220
Wright A. C., Tremmel M., Brooks A. M., Munshi F., Nagai D., Sharma R. S., Quinn T. R., 2021, MNRAS, 502, 5370
Yagi M., Koda J., Komiyama Y., Yamanoi H., 2016, ApJS, 225, 11
Yozin C., Bekki K., 2015, MNRAS, 452, 937
Zaritsky D., Donnerstein R., Dey A., Karunakaran A., Kadowaki J., Khim D. J., Spekkens K., Zhang H., 2023, ApJS, 267, 27

This paper has been typeset from a TEX/LATEX file prepared by the author.